

# JGR Planets

## RESEARCH ARTICLE

10.1029/2021JE006827

### Key Points:

- Parameters related to varying degrees of aqueous and thermal alteration can be identified in near- and midinfrared spectra of meteorites
- Combining observations across multiple wavelength ranges provides the most robust mineralogical determinations
- Spectral parameters associated with mineralogy and processing can help interpret results from Origins, Spectral Interpretation, Resource Identification, Security, Regolith Explorer (OSIRIS-REx) and Hayabusa2 observations

### Correspondence to:

H. C. Bates,  
[h.bates@nhm.ac.uk](mailto:h.bates@nhm.ac.uk)

### Citation:

Bates, H. C., Donaldson Hanna, K. L., King, A. J., Bowles, N. E., & Russell, S. S. (2021). A spectral investigation of aqueously and thermally altered CM, CM-AN, and CY chondrites under simulated asteroid conditions for comparison with OSIRIS-REx and Hayabusa2 observations. *Journal of Geophysical Research: Planets*, 126, e2021JE006827. <https://doi.org/10.1029/2021JE006827>

Received 15 JAN 2021

Accepted 28 MAY 2021

© 2021. The Authors.

This is an open access article under the terms of the [Creative Commons Attribution](#) License, which permits use, distribution and reproduction in any medium, provided the original work is properly cited.

# A Spectral Investigation of Aqueously and Thermally Altered CM, CM-An, and CY Chondrites Under Simulated Asteroid Conditions for Comparison With OSIRIS-REx and Hayabusa2 Observations

H. C. Bates<sup>1,2</sup> , K. L. Donaldson Hanna<sup>2,3</sup> , A. J. King<sup>1</sup>, N. E. Bowles<sup>2</sup> , and S. S. Russell<sup>1</sup>

<sup>1</sup>Department of Earth Sciences, Natural History Museum, London, UK, <sup>2</sup>Atmospheric, Oceanic and Planetary Physics, Oxford University, Oxford, UK, <sup>3</sup>Department of Physics, University of Central Florida, Orlando, FL, USA

**Abstract** Volatile-rich asteroids are crucial to understanding the transport of water and organics to the terrestrial planet forming region in the early Solar System. Observations of two such asteroids by Hayabusa2 and Origins, Spectral Interpretation, Resource Identification, Security, Regolith Explorer (OSIRIS-REx) suggest a relationship between these bodies and CI, CM, and CY chondrites. To confirm this, meteorite spectra need to be collected under appropriate conditions for comparison with asteroid observations. We report midinfrared (MIR) emissivity spectra (5.5–50  $\mu\text{m}$ ) obtained under ambient and simulated asteroid environment conditions and near-infrared (NIR) reflectance spectra (2–5  $\mu\text{m}$ ) of CM and CY chondrite fine-particulate (<35  $\mu\text{m}$ ) powders for which bulk mineralogy was determined using X-ray diffraction. Reflectance spectra show a 3  $\mu\text{m}$  feature associated with -OH/H<sub>2</sub>O that shifts from shorter (~2.72  $\mu\text{m}$ ) to longer (~2.90  $\mu\text{m}$ ) wavelengths and develops a rounder shape and reduced band area with increasing thermal metamorphism. In the MIR, the transparency feature (TF) and features in the Si-O bending region (>15  $\mu\text{m}$ ) can be used to infer the relative degree of aqueous alteration, and to resolve the effects of aqueous and thermal alteration, when combined with NIR spectral parameters. The MIR spectra of metamorphosed CY chondrites are distinct from CM chondrite spectra, including a plateau around the Christiansen feature (~8.00–12.50  $\mu\text{m}$ ) and features at longer wavelengths in the Si-O bending region (e.g., ~25.50  $\mu\text{m}$  compared to ~24.30  $\mu\text{m}$  in the CM spectra). We additionally report potential implications of the spectra and parameters determined in this study for the results from Hayabusa2 and OSIRIS-REx.

**Plain Language Summary** Some asteroids show evidence for once being exposed to water, and these bodies are thought to have contributed water to the Earth early in its evolution. We can observe some of these asteroids in our Solar System today, and a number of space missions have visited some of them with the aim of trying to find out more about their composition and history. Two of these missions, Hayabusa2 and OSIRIS-REx, have spectrometers, which can probe the surface mineralogy of the target asteroids. We can compare the data from these spectrometers to data we collect on Earth from meteorites, which we believe come from similar types of asteroids. In this study, we collected the spectra of meteorites which have undergone a variety of alteration and hence show a variety of compositions. We tried to tie features distinguishable in the spectra to the mineralogy, which we know well, so we have an example of what causes spectra to look a specific way. We can then look at Hayabusa2 and OSIRIS-REx spectra and see if they share any of the same features. That can give us an indication of what mineralogy may be present on the surfaces of their target asteroids.

## 1. Introduction

Asteroids offer an opportunity to investigate processes and events that occurred in the early Solar System. The C-complex asteroids show evidence for aqueous alteration (e.g., Lebofsky, 1980; Rivkin, 2002; Takir & Emery, 2012; Vilas, 1994) and may have played a role in the transport of volatiles into the terrestrial planet forming region of the protoplanetary disk (Alexander, 2017; Alexander et al., 2012; Barnes et al., 2016; Marty, 2012; Morbidelli et al., 2000). The JAXA mission Hayabusa2 (Tsuda et al., 2013) and the NASA mission Origins, Spectral Interpretation, Resource Identification, Security, Regolith Explorer (OSIRIS-REx; Lauretta et al., 2017) investigated C-complex asteroids: samples from the Cg-type asteroid Ryugu were returned to

Earth by Hayabusa2 in December 2020, and OSIRIS-REx collected a sample from the surface of the B-type asteroid Bennu in October 2020 that will be returned to Earth in 2023. The aim of both missions is to understand the origin and evolution of volatile-rich bodies in the Solar System.

Analysis of the global near-infrared (NIR) spectrum of Ryugu shows a low albedo and a weak (band depth of 7%–10%) 3  $\mu\text{m}$  feature (indicative of -OH, the position of the feature is most consistent with Mg-phyll-silicates), leading to the suggestion that materials on the asteroid surface experienced either a low degree of aqueous alteration or hydration followed by thermal alteration and dehydration (Kitazato et al., 2019, 2021). In contrast, the NIR spectrum of Bennu shows a deeper 3  $\mu\text{m}$  feature than Ryugu, suggesting that hydrated mineral phases are widespread on the surface (Hamilton et al., 2019). The Bennu spectrum also has a feature at 3.4  $\mu\text{m}$  consistent with organics and carbonates (calcite) that likely reflect a high degree of aqueous alteration (Kaplan et al., 2020; Simon et al., 2020). Mid-infrared (MIR) spectra of the Bennu surface support this conclusion as they are dominated by phyllosilicate vibrational features, while magnetite vibrational bands, a common mineral in highly altered meteorites (King et al., 2015, 2017), have also been detected at  $\sim 18.0$  and  $\sim 29.4$   $\mu\text{m}$  (Hamilton et al., 2019).

Spectral properties indicate that materials on Ryugu may be similar to the aqueously and thermally altered CM and CY chondrite meteorites (King, Bates, et al., 2019; Kitazato et al., 2019), whereas Bennu is more closely related to the aqueously altered CM and CI chondrites (Hamilton et al., 2019). The CI and CM chondrites are among the most primitive extraterrestrial materials available to study on Earth. CI1 chondrites are highly aqueously altered and dominated (>80 vol%) by phyllosilicates, with little (<5 vol%) remaining unaltered primary anhydrous silicate (e.g., King et al., 2015). The aqueously altered CM chondrites show a wider range of petrologic types from 2 to 1, and have phyllosilicate abundances of 60–90 vol% and primary silicate abundances of <10–30 vol% (e.g., Brearley, 2006; Endress et al., 1996; King et al., 2017; Tomeoka & Buseck, 1985). In contrast, following aqueous alteration, thermally altered CM chondrites reached peak metamorphic temperatures of  $\sim 300$ – $>750^\circ\text{C}$  resulting in the dehydration of phyllosilicates and recrystallization back into secondary silicates. These secondary recrystallized silicates typically have lower crystallinity and compositions that are more Fe-rich than the primary, anhydrous silicate phases (e.g., King et al., 2015; King, Bates, et al., 2019; Nakamura, 2005; Tonui et al., 2014). For clarity, throughout this study, the terms anhydrous and primary refer to phases which were never aqueously altered, while dehydrated, recrystallized, and secondary refer to phases which were aqueously and then thermally altered.

The CY chondrites are a newly described group containing samples originally thought to be thermally altered CI chondrites, but later shown to have distinct characteristics to both CI and CM chondrites (Ikeda, 1992; King, Russell, et al., 2019). These meteorites have experienced high degrees of both aqueous and thermal alteration (reaching peak temperatures of  $500$ – $750^\circ\text{C}$ ). As with thermally altered CM chondrites, the CYs contain abundant dehydrated phyllosilicate and/or recrystallized silicate phases. In contrast to CM and CI chondrites, all CYs show high sulfide abundances (12–29 vol%) (King, Russell, et al., 2019; Tonui et al., 2014). By comparing remotely collected Ryugu and Bennu spectra with laboratory meteorite spectra, we can interpret the primitive asteroid surface mineralogy and infer the processes and alteration that occurred during the body's evolution. Furthermore, we can compare Ryugu and Bennu to other volatile-rich asteroids that have previously been linked to these aqueously and thermally altered meteorites (Burbine et al., 2002; Clark et al., 2010; Fornasier et al., 2016; Hiroi et al., 1993; Rivkin et al., 2003; Takir et al., 2015; Vilas et al., 1994; Ziffer et al., 2011).

In order to identify materials similar to CM, CI, and CY chondrites present on the surfaces of volatile-rich asteroids, particularly Ryugu and Bennu, we require IR spectra of these meteorites that are directly comparable to Hayabusa2 and OSIRIS-REx observations. For example, Hayabusa2 has the near-infrared spectrometer (NIRS3) covering the 1.8–3.2  $\mu\text{m}$  spectral range (Iwata et al., 2017) and the Mobile Asteroid Scout (MASCOT) Radiometer (MARA; Grott et al., 2017), which has several channels covering the MIR (5–15.5  $\mu\text{m}$ ). OSIRIS-REx has the OSIRIS-REx Visible and Infrared Spectrometer covering 0.4–4.3  $\mu\text{m}$  (OVIRS; Reuter et al., 2018) and the OSIRIS-REx Thermal Emission Spectrometer covering 5.7–50  $\mu\text{m}$  (OTES; Christensen et al., 2018). The MIR wavelength range is particularly crucial, as it is where many rock forming minerals show diagnostic features related to mineralogy, however remote asteroid observations are dominated by emission in this region, and the positions and shapes of spectral features in emissivity spectra are affected by grain size, porosity and the presence of thermal gradients in the upper surface layers

on airless bodies (Donaldson Hanna, Wyatt, et al., 2012; Donaldson Hanna, Thomas, et al., 2012; Donaldson Hanna et al., 2019; Henderson & Jakosky, 1994; Logan et al., 1973; Salisbury & Walter, 1989; Thomas et al., 2010). Therefore, to accurately compare laboratory data to OTES and other remote observations, MIR emissivity spectra of meteorites need to be collected under appropriate simulated asteroid environment (SAE) conditions.

We have collected MIR emissivity spectra between 5.5 and 50  $\mu\text{m}$  from powdered samples of 12 CM and CY chondrites under both ambient and SAE conditions (Donaldson Hanna et al., 2019, 2021). The mineralogy of the same meteorite powders was characterized using X-ray diffraction (XRD) so that spectral parameters can be directly related to the specific compositions and alteration history of the samples. In addition, we collected reflectance spectra from the powders across the 2–5  $\mu\text{m}$  region. This wavelength range encompasses the 3  $\mu\text{m}$  vibrational feature, which is due to -OH and varies in position based on the cation the hydroxyl is bonded to, giving an indication of hydrated mineral composition (Beck et al., 2010; Rivkin, 2002; Takir et al., 2013). Combining these spectral measurements with the known mineralogical properties of meteorites provides a useful tool for interpreting results from Hayabusa2 and OSIRIS-REx and understanding the history of Ryugu, Bennu, and other volatile-rich asteroids.

## 2. Experimental

### 2.1. Samples

We investigated 12 meteorites representing a range of aqueous and thermal alteration. In this study, we use the scale developed by Nakamura (2005) using XRD, scanning electron microscopy (SEM) and transmission electron microscopy (TEM) to describe thermal alteration. This scale has four stages describing peak metamorphic temperature: stage I (<250°C), stage II (250–500°C), stage III (500–750°C), and stage IV (>750°C). Of the 12 samples, seven are classified as CM chondrites that experienced no heating to severe metamorphism; the CM2s Alan Hills (ALH) 83100, ALH 83102, and Lonewolf Nunataks (LON) 94101 are all aqueously altered and have not experienced thermal alteration; the CM2s Elephant Moraine (EET) 96029 and Yamato (Y) 793321 experienced aqueous alteration followed by moderate thermal alteration (temperatures of 300–500°C, stage II (Lee et al., 2016; Nakamura, 2006)); and Pecora Escarpment (PCA) 02010 and PCA 02012, which experienced aqueous alteration followed by severe heating at temperatures of >750°C (stage IV [Alexander et al., 2013; Hanna et al., 2020; King et al., 2021; Mahan et al., 2018]). We also investigated the CM-anomalous (CM-an) chondrite Wisconsin Range (WIS) 91600, which has experienced aqueous alteration followed by thermal alteration to ~300–500°C (stage II) but shows a high magnetite abundance (~7 vol%) and affinities with CI chondrites (Howard et al., 2015; Tonui et al., 2014). In addition, we investigated the stage III (500–750°C) CY Y 980115 and the stage IV CYs Belgica (B) 7904, Y 86720, and Y 86789 (the latter two likely paired, Matsuoka et al., 1996).

### 2.2. X-Ray Diffraction

Mineral abundances were determined using position-sensitive-detector X-ray diffraction (PSD-XRD) at the Natural History Museum, London. Chips of each meteorite (~1.8 g) were ground to a particle size of <35  $\mu\text{m}$  using an agate mortar and pestle. Approximately 50 mg of powdered sample was packed into an aluminum sample well with the sharp edge of a stainless-steel spatula and analyzed using an Enraf-Nonius PDS120 X-ray diffractometer with an INEL curved 120° PSD. For each meteorite, diffraction patterns were collected from two subsamples (HB1 and HB2) of ~50 mg taken from the original 1.8 g powder.

The PSD is in a static geometry relative to the X-ray beam and sample stage, the latter of which was rotated continuously throughout an analysis. Cu K $\alpha_1$  radiation was selected using a Ge 111 monochromator and the size of the beam on the sample was restricted to 0.24  $\times$  2 mm using post monochromator slits. The beam flux of the instrument was monitored at regular intervals using a polished Fe-metal block and varied <1% over the experimental run. Diffraction patterns were collected from the meteorite samples for 16 h, and from mineral standards prepared in the same way for 30 min.

Mineral abundances were determined using a profile-stripping technique (Cressey & Schofield, 1996), which has been used to investigate the mineralogy of CI, CM, CO, CV, CR, and CY chondrites (Alexander

et al., 2018; Bland et al., 2004; Hanna et al., 2020; Howard et al., 2009, 2011, 2015; King et al., 2015; King, Bates, et al., 2019; King, Russell, et al., 2019; Lee et al., 2016). The XRD patterns of mineral standards were scaled to the same measurement time as the meteorite patterns (e.g., 30 min  $\times$  32 = 16 h), and then reduced by a factor so that peaks in the standard pattern were the same intensity as the respective peaks in the meteorite pattern. The mineral standard pattern was then subtracted from the meteorite pattern to leave a residual. This process was repeated for all phases identified in the meteorite patterns until there were zero counts in the residual. The fit factors were then corrected for relative differences in X-ray absorption to give a volume fraction. Previous studies using the profile stripping method have applied a linear least squares routine to fit the standard patterns to the meteorite patterns in order to determine detection limits and uncertainties in mineral abundances (King et al., 2015; Schofield et al., 2002). This process found similar mineral standard factors that were identified in the profile-stripping method and yielded detection limits of 0.5–1 vol% and absolute uncertainties in the abundances of 1–1.5 vol%. A petrologic type based on the phyllosilicate fraction (PSF) could then be determined from the modal mineralogy. This expresses the degree of aqueous alteration as the volume of phyllosilicates divided by the abundance of phyllosilicates plus anhydrous silicates. This gives a petrologic type, with a PSF of <0.05 as type 3.0 and >0.95 as type 1 (Howard et al., 2015).

### 2.3. NIR Reflectance Spectra

NIR reflectance spectra (2–5  $\mu\text{m}$ ) were collected using a Bruker VERTEX 70v Fourier Transform Infrared Spectrometer (FTIR) in bidirectional reflectance geometry with a Specac Selector diffuse reflectance accessory at the Planetary Spectroscopy Facility at the University of Oxford. All observations were obtained under vacuum ( $\sim 2$  hPa) at a spectral resolution of 4  $\text{cm}^{-1}$ , and the resulting spectra are the average of 250 scans. A wide range mid- to far-IR (MIR-FIR) beam splitter (T240/3) and a room temperature deuterated L-alanine doped triglycine sulfate (RT-DLaTGS) detector were used. Approximately 200 mg of meteorite powder was spooned into the sample cups. The flat edge of a spatula was drawn across the surface to create a nearly flat surface without compressing the uppermost layers of the sample. Spectra were collected after the samples had been heated to  $\sim 150^\circ\text{C}$  for 2 h in a vacuum oven in order to reduce the effect of terrestrially adsorbed water (Bates et al., 2020). To remove instrument effects, each meteorite spectrum was divided through by the spectrum of a diffuse gold calibration target measured under the same analytical conditions.

The position of the 3  $\mu\text{m}$  feature was determined by first isolating the spectral region of interest, and then smoothing it with a moving average of 10–15, sufficient to reduce the noise without modifying the spectral shape. A wavelength grid was generated across the region with an increment of  $2 \times 10^{-4}$   $\mu\text{m}$  and a fourth order polynomial was fit across the center of the feature, with the position established as the point of minimum or maximum reflectance of the polynomial (Bates et al., 2020; Donaldson Hanna, Wyatt, et al., 2012; Donaldson Hanna, Thomas, et al., 2012). The area of the  $\sim 3$   $\mu\text{m}$  band was calculated as the area between the straight-line continuum (fitted between 2.65 and 3.87  $\mu\text{m}$ ) and the continuum normalized spectrum. The uncertainties are presented as one standard deviation, representing variability from the average of calculated parameters.

### 2.4. MIR Emissivity Spectra

MIR emissivity spectra were collected in the Planetary Analog Surface Chamber for Asteroid and Lunar Environments (PASCALE; Donaldson Hanna et al., 2021) at the Planetary Spectroscopy Facility. PASCALE is mounted to the same Bruker VERTEX 70v FTIR that NIR reflectance spectra were collected in, and the same T240/3 beam splitter and RT-DLaTGS detector were used. There is a region of low signal throughput of the beam splitter near  $16 \pm 0.1$   $\mu\text{m}$ , resulting in low signal to noise data in this region (Donaldson Hanna et al., 2021). Features at  $\sim 16$   $\mu\text{m}$  were therefore not considered in this study. Measurements were collected under ambient and SAE conditions. Sample cups are designed so that under SAE conditions, the thermal gradients expected on an airless body (e.g., Donaldson Hanna, Wyatt, et al., 2012; Donaldson Hanna, Thomas, et al., 2012; Donaldson Hanna et al., 2019, 2021; Hanna et al., 2020; Henderson & Jakosky, 1994; Logan et al., 1973; Thomas et al., 2010, 2012) are replicated and also to create an area within the sample cup that has a nearly homogeneous thermal gradient for sampling by the spectrometer. The cup requires  $\sim 1.8$  g of material to be filled fully, and the same powders for which PSD-XRD and NIR reflectance spectroscopy were



collected were used for emissivity spectral analysis. As with the NIR reflectance measurements, meteorite powder was transferred into the sample cups and flattened without compressing the uppermost layers. This is particularly important as the spectral contrast of MIR features can be affected by the reduction in porosity caused by any compression of the material (Salisbury, 1993).

Under ambient conditions, the environment chamber is backfilled with dry nitrogen gas ( $N_2$ ) to an atmospheric pressure of  $\sim 1,000$  mbar and maintained at an ambient temperature. Under SAE conditions, the near-surface environment of an airless body is simulated by removing atmospheric gasses to a vacuum ( $<10^{-4}$  mbar), cooling the interior of the chamber to  $<150^\circ\text{C}$  using liquid  $N_2$  and heating samples from above by a quartz-halogen lamp attached to the outside of the chamber, and below by a sample cup heater until the maximum brightness temperature of the sample is  $\sim 75^\circ\text{C}$  (Donaldson Hanna et al., 2021). This induces a thermal gradient in the upper hundreds of microns of the sample, which is what we would expect on the surface of Bennu near local midday (Hergenrother et al., 2014). Samples were kept in the chamber while the experimental set up is changed between ambient and SAE conditions to ensure the same optical surface is observed. Spectra were collected from  $\sim 5.5$  to  $50\ \mu\text{m}$  at a resolution of  $4\ \text{cm}^{-1}$  and are the average of 250 scans. During the experimental run, daily measurements of a black body target were made at two temperatures that bracket the sample temperature ( $\sim 67^\circ\text{C}$  and  $\sim 87^\circ\text{C}$ ) to generate an instrument response function, which was used to calibrate the data to effective emissivity. The methods used to calibrate the sample measurements are based on published methods (e.g., Ruff et al., 1997; Thomas et al., 2012). For more details on the calibration methods and radiometric accuracy of PASCALE, see Donaldson Hanna et al. (2021). During analysis, diagnostic spectral feature positions were identified using the same methodology as described for the  $3\ \mu\text{m}$  feature above.

### 3. Results

#### 3.1. X-Ray Diffraction

Figure 1a shows a PSD-XRD pattern for the CM chondrite ALH 83100. This pattern has diffraction peaks at  $\sim 12^\circ$  and  $\sim 25^\circ$ , consistent with Fe-cronstedtite, and broad features near  $\sim 19^\circ$  and  $\sim 61^\circ$  that we attribute to Mg-serpentine. These peaks are typical of aqueously altered CM chondrites (Howard et al., 2009, 2011, 2015; King et al., 2017), and the ALH 83100 pattern shown in Figure 1a is similar to the ALH 83102 (paired with ALH 83100, Grossman, 1994) and LON 94101 diffraction patterns collected in this study. The subsamples (HB1 and HB2) of ALH 83100, ALH 83102, and LON 94101 showed little variation in mineralogy within each meteorite (Table 1), demonstrating that the original 1.4 g powder was homogenized. The modal mineralogy for the aqueously altered CM samples are 79–87 vol% phyllosilicate, 7–10 vol% olivine, 1–4 vol% enstatite, 2–5 vol% magnetite,  $\sim 1$  vol% Fe-sulfide, and  $\sim 1$  vol% carbonate. The PSF petrologic types of these CMs are 1.2–1.3, indicating a high degree of aqueous alteration.

Figure 1a also shows representative PSD-XRD patterns from a stage II (EET 96029) and stage IV (PCA 02010) CM chondrite. The stage II EET 96029 and Y 793321 patterns show diffraction peaks due to primary olivine, enstatite, gypsum, calcite, magnetite, and Fe-sulfide, but do not show diffraction peaks associated with phyllosilicates. During the profile stripping of the stage II CMs, following removal of the crystalline phases there was a remaining residual greater than zero and the sum of the fit factors was less than one. This indicated the samples had a significant noncrystalline component, which has also been observed previously in the PSD-XRD patterns of thermally altered CM samples (King, Russell, et al., 2019; Lee et al., 2016). We cannot rule out the presence of amorphous, primitive silicates or poorly crystalline Fe-(oxy)hydroxides and rusts, however the residual patterns were generally in good agreement with the overall shape and intensity of the scaled phyllosilicate patterns (excluding the diffraction peaks). Dehydration and dehydroxylation of phyllosilicates cause the loss of interlayer  $H_2O$  and structural  $-OH$ , and the formation of a highly disordered and/or very fine-grained phase, therefore we attribute the remaining counts in the residual to dehydrated phyllosilicates. The modal mineralogy for the stage II CMs is 10–12 vol% primary olivine, 6–9 vol% enstatite, 1–2 vol% magnetite,  $\sim 1$  vol% Fe-sulfide,  $\sim 1$  vol% carbonate,  $<1$  vol% metal, and 76–81 vol% disordered phyllosilicate (Table 1). King et al. (2021) showed a PSF petrologic type could be determined for a dehydrated CM chondrite if all disordered phyllosilicate and recrystallized phases were assumed to be hydrous phyllosilicates in the premetamorphosed mineralogy. EET 96029 and Y 793321 have petrologic types of 1.4–1.5.

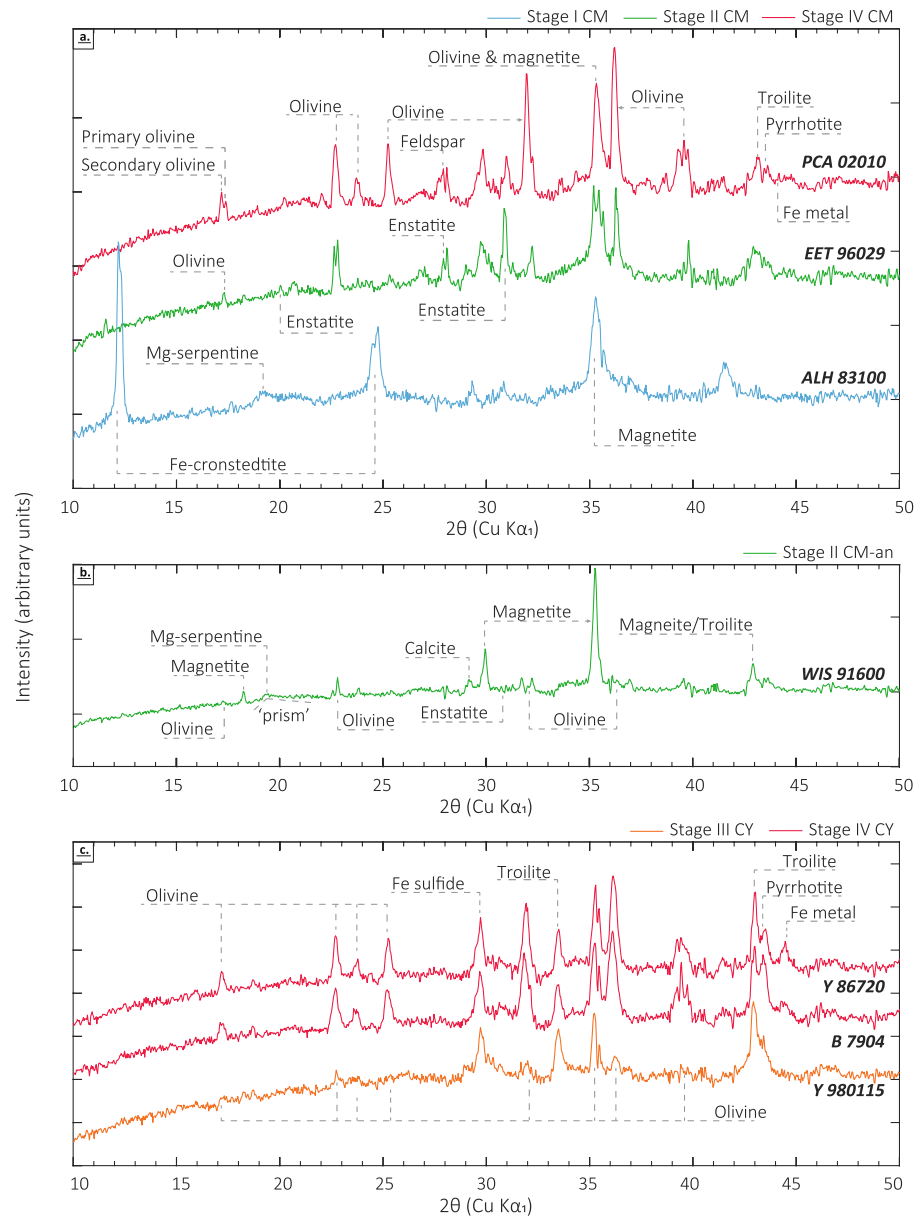


**Figure 1.** Position-sensitive-detector X-ray diffraction (PSD-XRD) patterns (a) the aqueously altered CM Alan Hills (ALH) 83100, the stage II CM Elephant Moraine (EET) 96029 and the stage IV CM Pecora Escarpment (PCA) 02012; (b) the stage II CM-an Wisconsin Range (WIS) 91600; and (c) the stage III CY Y 980115 and the stage IV CYs B 7904 and Y 86720. Due to the similarity between patterns of the same petrologic type/heating stage, only representative patterns are included in the figure. Patterns are offset on the y axis.

The stage IV CM patterns show similar diffraction peaks to the stage II patterns but with the addition of some broad, Fe-rich olivine peaks. The broad peaks indicate poorly crystalline phases, and this and the chemistry of the olivine suggests they are secondary phases which have recrystallized from the dehydrated phyllosilicate during thermal alteration. During profile stripping, following the removal of crystalline phases there was a noncrystalline component identified in PCA 02012 but not in PCA 02010, indicating the latter contained no disordered phyllosilicates. Their modal mineralogy of PCA 02010 and PCA 02012 is 13–27 vol% primary olivine, 20–63 vol% secondary olivine, 14–16 vol% enstatite, 8–9 vol% Fe-sulfide, 1–2 vol% feldspar, and <1 vol% metal. PCA 02012 also contains ~28 vol% disordered phyllosilicate and minor (<1 vol%) carbonate (Table 1). Previous analysis of different samples of PCA 02012 by Hanna et al. (2020) showed no

**Table 1**  
Modal Mineralogy Determined From Position-Sensitive-Detector X-Ray Diffraction (PSD-XRD). Also Included are the Phyllosilicate Fraction (PSF) Petrologic Types Determined From the Mineralogy and the Heating Stage in the Nakamura (2005) Scheme

Meteorite	Subsample	Classification	Primary olivine (vol%)	Secondary olivine (vol%)	Enstatite (vol%)	Magnetite (vol%)	Sulfide (vol%)	Carbonates (vol%)	Gypsum (vol%)	Feldspar (vol%)	Metal (vol%)	Phyllosilicate (vol%)	Dehydrated phyllosilicate (vol%)	PSF petrologic type	Heating stage
ALH 83100 (306)	HB1	CM1/2	10	-	4	5	1	1	-	-	-	79	-	1.3	-
	HB2	CM1/2	7	-	3	4	1	1	-	-	-	84	-	1.2	-
ALH 83102 (92)	HB1	CM2	8	-	3	3	1	1	-	-	-	84	-	1.3	-
	HB2	CM2	7	-	1	3	1	1	-	-	-	87	-	1.2	-
LON 94101 (113)	HB1	CM2	9	-	3	2	1	1	-	-	-	85	-	1.3	-
	HB2	CM2	9	-	3	2	1	1	-	-	-	87	-	1.3	-
EET 96029 (82)	HB1	CM2	11	-	9	2	1	<1	1	-	<1	-	76	1.5	2
	HB2	CM2	10	-	6	2	1	<1	1	-	<1	-	80	1.4	2
Y 793321 (53)	HB1	CM2	12	-	7	2	1	1	-	-	<1	-	76	1.5	2
	HB2	CM2	10	-	6	1	1	1	-	-	<1	-	81	1.4	2
PCA 02010 (28)	HB1	CM2	16	58	16	-	8	-	-	2	<1	-	-	1.8	4
	HB2	CM2	13	63	15	-	8	-	-	1	<1	-	-	1.7	4
PCA 02012 (28)	HB1	CM2	27	21	15	-	8	1	-	1	<1	-	27	2.0	4
	HB2	CM2	27	20	14	-	9	1	-	1	<1	-	28	2.0	4
WIS 91600 (76)	HB1	CM-an	10	-	3	9	4	1	-	-	-	-	73	1.4	2
	HB2	CM-an	14	-	2	9	3	1	-	-	-	-	70	1.4	2
Y 980115 (62)	HB1	C11/CY	-	8	-	2	12	-	-	-	<1	-	78	1.0	3
	HB2	C11/CY	-	8	-	2	10	-	-	-	<1	-	80	1.0	3
B 7904 (63)	HB1	C2-ung/CY	23	51	8	-	18	-	-	-	1	-	-	1.8	4
	HB2	C2-ung/CY	27	49	10	-	11	2	-	-	1	-	-	1.9	4
Y 86720 (54)	HB1	C2-ung/CY	-	60	5	-	33	-	-	-	2	-	-	1.2	4
	HB2	C2-ung/CY	-	57	11	-	30	-	-	-	2	-	-	1.4	4
Y 86789 (70)	HB1	C2-ung/CY	-	60	5	-	32	-	-	-	3	-	-	1.2	4
	HB2	C2-ung/CY	-	62	5	-	31	-	-	-	2	-	-	1.2	4

Abbreviations: ALH, Alan Hills; EET, Elephant Moraine; LON, Lonerwolf Nunataks; PCA, Pecora Escarpment; WIS, Wisconsin Range.

dehydrated phyllosilicates, indicating the meteorite is heterogeneous with some areas potentially having experienced higher degrees of thermal alteration. The stage IV CMs have PSF petrologic types of 1.7–2.0.

Figure 1b shows the PSD-XRD pattern of the CM2 WIS 91600. A “prism” feature associated with dehydrated Mg-rich serpentines and smectites is also resolvable (Che et al., 2011; Nakamura, 2005; Tonui et al., 2014). The modal mineralogy of WIS 91600 is ~12 vol% primary olivine, ~3 vol% enstatite, ~9 vol% magnetite, ~4 vol% Fe-sulfide, ~1 vol% calcite, and ~72 vol% phyllosilicate, with a PSF petrologic type of 1.4. The HB1 and HB2 subsamples of WIS 91600 gave results that were within error of one another (Table 1), and the mineralogy is consistent with previous analysis of a different sample of WIS 91600 by Howard et al. (2015).

PSD-XRD patterns for representative stage III and stage IV CYs are shown in Figure 1c. The stage III CY Y 980115 contains ~8 vol% secondary olivine, ~2 vol% magnetite, ~11 vol% Fe-sulfide, and ~79 vol% dehydrated phyllosilicate (Table 1). Y 980115 has a PSF petrologic type of 1.0, as it contains no primary silicates. This is consistent with the previously determined mineralogy of stage III CYs (King et al., 2015; King, Bates, et al., 2019). The stage IV CY B 7904 contains ~25 vol% primary olivine, ~50 vol% secondary olivine, ~9 vol% enstatite, ~14 vol% Fe-sulfide, <2 vol% calcite, and ~1 vol% metal, giving a PSF petrologic type of 1.9. This is consistent with previous investigations of B 7904 (King, Bates, et al., 2019). The modal mineralogy of the stage IV CYs Y 86720 and Y 86789 are 58–63 vol% secondary olivine, 5–11 vol% enstatite, 28–33 vol% Fe-sulfide, and 2–3 vol% Fe-metal. The multiple subsamples of B 7904, Y 86720, and Y 86789 produced similar mineralogies, apart from a difference of 7 vol% in the Fe-sulfide abundance in the B 7904 subsamples and a difference in enstatite abundance of 6 vol% in the Y 86720 subsamples.

### 3.2. Aqueously Altered CM Chondrites

#### 3.2.1. NIR Reflectance Spectral Features

All aqueously altered CM spectra show a large, asymmetric absorption feature between ~2.70–4.00  $\mu\text{m}$  (Figure 2a, Table 2), suggesting they all contain -OH or  $\text{H}_2\text{O}$ . As the samples were heated prior to measurement, and spectra were collected under vacuum, we attribute these features to the presence of hydrated mineral phases rather than adsorbed terrestrial water. There may still be some water trapped in high-energy sites contributing to the 3  $\mu\text{m}$  feature (Beck et al., 2010), however thermogravimetric analysis (TGA) shows most of the molecular and mesopore water is removed on heating up to 150–200°C (Garenne et al., 2014). The spectra of ALH 83100 and ALH 83102 show sharp features with minima at 2.72  $\mu\text{m}$  and band areas of 0.16 and 0.14  $\mu\text{m}^{-1}$ , respectively (Table 2). The shape and position of the features are consistent with the 3  $\mu\text{m}$  features in the spectra of Mg-serpentine standards and in the spectra of other CM2 chondrites (Bates et al., 2020; Takir et al., 2013). LON 94101 shows multiple minima at 2.72 and 2.80  $\mu\text{m}$ , with a band area of 0.14  $\mu\text{m}^{-1}$ , the former feature due to Mg-serpentine and the latter consistent with Fe-cronstedtite (e.g., Bates et al., 2020).

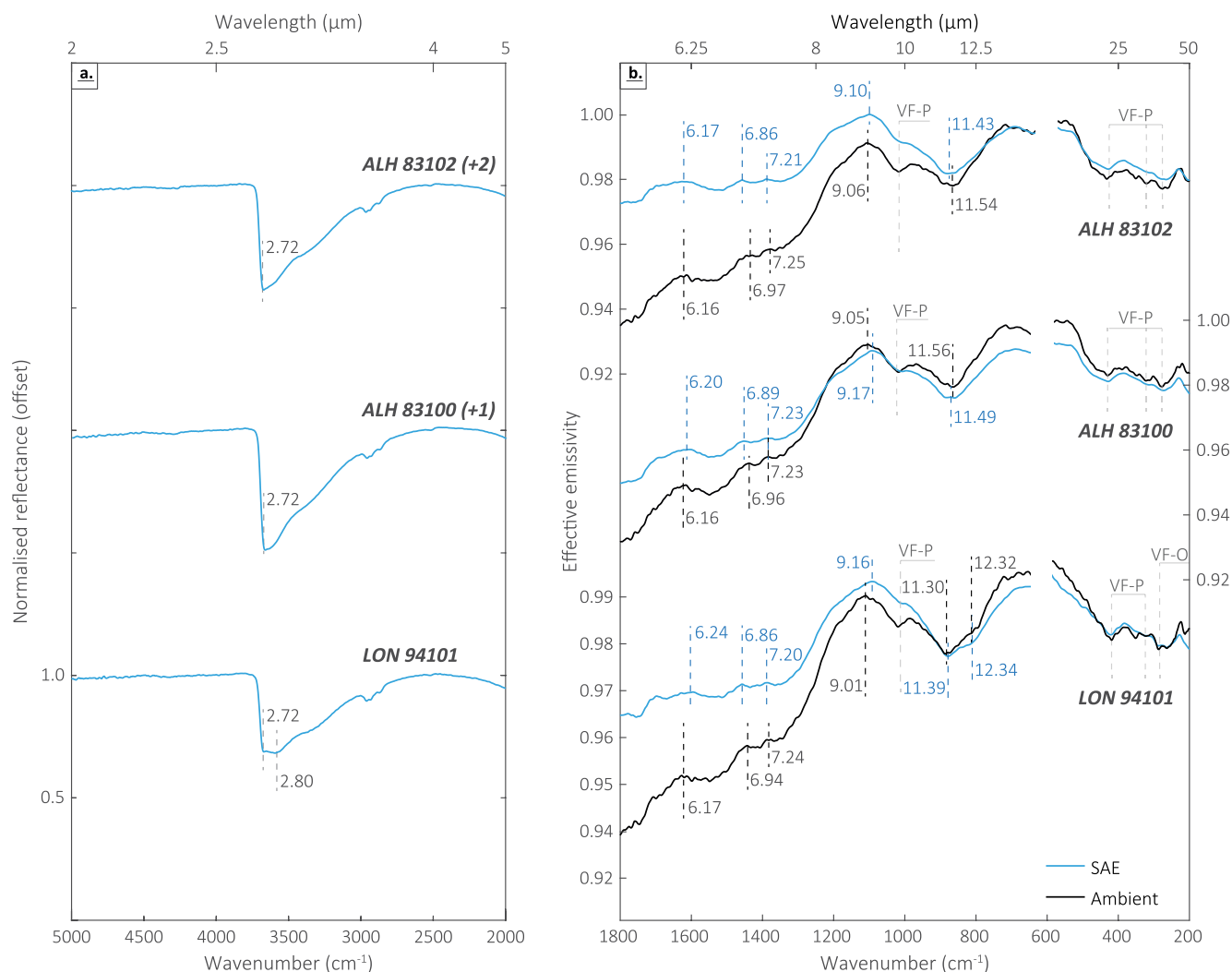
#### 3.2.2. Ambient and SAE MIR Spectral Features

Figure 2b shows the ambient (black) and SAE (blue) emissivity spectra of the aqueously altered CM chondrites (ALH 83100, ALH 83102, and LON 94101). The positions of the diagnostic features identified in the spectra are given in Table 3. The ambient emissivity spectra of the aqueously altered CM chondrites show vibrational features in the 5–8  $\mu\text{m}$  range near 6.16, 6.95, and 7.24  $\mu\text{m}$ . The 6.16  $\mu\text{m}$  feature is consistent with both phyllosilicates and bound molecular water (Bates et al., 2020), and the 6.95 and 7.24  $\mu\text{m}$  features are consistent with carbonates (Beck et al., 2018).

The CM ambient emissivity spectra show Christiansen features (CF) between 9.01 and 9.05  $\mu\text{m}$ , and transparency features (TF) at 11.43–11.56  $\mu\text{m}$ . The TF in the LON 94101 ambient emissivity spectrum has a slight doublet shape with an additional minimum at 12.32  $\mu\text{m}$ . Following the trend established in McAdam et al. (2015), whereby the TF moves to shorter wavelengths with increasing aqueous alteration, this doublet in the emissivity spectra suggests that it has experienced less aqueous alteration than ALH 83100 and ALH 83102, consistent with the petrologic type (1.3 vs. 1.2) of these meteorites (Table 1).

The ambient emissivity spectra of ALH 83100, ALH 83102, and LON 94101 show fundamental vibrational features near 9.83 and 23.27  $\mu\text{m}$ . These are phyllosilicate Si-O stretching and Si-O bending vibrational features, respectively (Farmer, 1974; Michalski et al., 2006). The Si-O bending feature in the LON 94101





**Figure 2.** (a) The near-infrared (NIR) reflectance spectra between 2 and 5  $\mu\text{m}$  for the aqueously altered CMs Alan Hills (ALH) 83100, ALH 83102, and Lonewolf Nunataks (LON) 94101. Spectra are normalized to a linear continuum fitted to points on either side of the feature (2.65–3.87  $\mu\text{m}$ ) and offset by the value given in brackets next to the meteorite name. (b) The midinfrared (MIR) emissivity spectra between 5.5 and 50  $\mu\text{m}$  for the same meteorites collected under ambient (black) and simulated asteroid environment (SAE) (blue) conditions. VF-P refers to vibrational features associated with phyllosilicates, and VF-O refers to vibrational features associated with olivine. Gaps in the spectra are a region of low signal to noise due to low beam splitter throughput.

emissivity spectrum is at slightly longer wavelengths (23.76  $\mu\text{m}$ ) than in the ALH 83100 and ALH 83102 spectra (Table 3). The trend determined by Hanna et al. (2020) suggests that the Si-O bending minimum moves to shorter wavelengths with increasing aqueous alteration, again implying that LON 94101 is less aqueously altered. Between 25 and 50  $\mu\text{m}$ , the ALH 83100 and ALH 83102 emissivity spectra show phyllosilicate vibrational features near 31.26 and 36.65  $\mu\text{m}$  and the LON 94101 emissivity spectra shows features at 31.15 and 34.93  $\mu\text{m}$ ; the former is due to phyllosilicates, and the latter is more consistent with olivine (Bates et al., 2020; Bishop et al., 2008; Hamilton, 2010; Lane et al., 2011).

Emissivity spectra of the CMs collected under SAE show some differences to the ambient spectra (Figure 2b). For example, there is a slight shift (of up to 0.16  $\mu\text{m}$ ) to longer wavelengths of the CF. This is consistent with results from Donaldson Hanna et al. (2021), who also observed a shift to longer wavelengths of the CF in the spectra of a sample of ALH 83100, but is in contrast to the study of Donaldson Hanna et al. (2019), who reported a shift of the CF to shorter wavelengths in the spectra of both hydrated physical mixtures and hydrated meteorites collected under similar SAE conditions. In addition, for all aqueously altered CM spectra we observe a decrease in spectral contrast between 5 and 8  $\mu\text{m}$ , and a reduction in contrast of some of the vibrational features between 16.7 and 50.0  $\mu\text{m}$ , most notably the feature near 31.25  $\mu\text{m}$ .

**Table 2**  
*The Near Infrared (NIR) Spectral Parameters*

Meteorite	Classification	Heating Stage	3 $\mu\text{m}$ feature ( $\mu\text{m}$ )	3 $\mu\text{m}$ feature area ( $\mu\text{m}^{-1}$ )
ALH 83100	CM1/2	-	$2.72 \pm 0.01$	$0.16 \pm 0.04$
ALH 83102	CM2	-	$2.72 \pm 0.01$	$0.14 \pm 0.04$
LON 94101	CM2	-	$2.80 \pm 0.01$	$0.14 \pm 0.03$
EET 96029	CM2	2	$2.93 \pm 0.01$	$0.08 \pm 0.01$
Y 793321	CM2	2	$2.88 \pm 0.01$	$0.05 \pm 0.01$
PCA 02010	CM2	4	$3.02 \pm 0.04$	$0.17 \pm 0.01$
PCA 02012	CM2	4	$2.94 \pm 0.01$	$0.15 \pm 0.01$
WIS 91600	CM-an	2	$2.90 \pm 0.01$	$0.04 \pm 0.01$
Y 980115	CI1/CY	3	$2.89 \pm 0.01$	$0.07 \pm 0.01$
B 7904	C2-ung/CY	4	$2.90 \pm 0.01$	$0.03 \pm 0.01$
Y 86720	C2-ung/CY	4	$2.91 \pm 0.01$	$0.07 \pm 0.01$
Y 86789	C2-ung/CY	4	$2.91 \pm 0.01$	$0.05 \pm 0.01$

Abbreviations: ALH, Alan Hills; EET, Elephant Moraine; LON, Lonewulf Nunataks; PCA, Pecora Escarpment; WIS, Wisconsin Range.

### 3.3. Aqueously and Thermally Altered CM Chondrites

#### 3.3.1. NIR Reflectance Spectral Features

Figure 3a shows the 3  $\mu\text{m}$  region for the stage II CM chondrites EET 96029 and Y 793321 and the stage IV CM chondrites PCA 02010 and PCA 02012. All show an asymmetric feature and with band center minima at longer wavelengths than those observed in the aqueously altered CM spectra. The spectra of the stage II CMs EET 96029 and Y 793321 show features at 2.93 and 2.88  $\mu\text{m}$ , and band areas of 0.08 and 0.05  $\mu\text{m}^{-1}$ , respectively. Stage IV CM spectra show features at 3.02 and 2.94  $\mu\text{m}$ , and band areas of 0.17 and 0.15  $\mu\text{m}^{-1}$  for PCA 02010 and PCA 02012, respectively.

#### 3.3.2. Ambient and SAE MIR Spectral Features

Figures 3b and 3c show the ambient (black) and SAE (green/red) emissivity spectra of the stage II and stage IV CM chondrites. In the 5–8  $\mu\text{m}$  range the stage II CMs EET 96029 and Y 793321 show weak features compared to the aqueously altered CM ambient emissivity spectra. The stage IV CMs PCA 02010 and PCA 02012, which have undergone intense thermal metamorphism on their parent bodies, show peaks in their ambient emissivity spectra near 6.10  $\mu\text{m}$  (Figure 3c). The EET 96029 and Y 793321 ambient emissivity spectra show CFs and TFs at 8.86 and 8.89  $\mu\text{m}$ , and at 12.47 and 12.54  $\mu\text{m}$ , respectively. The PCA 02010 and PCA 02012 ambient spectra show CFs and TFs at 8.75 and 8.67  $\mu\text{m}$ , and at 12.45 and 12.50  $\mu\text{m}$ .

The ambient emissivity spectra of the stage II and stage IV CMs show vibrational features consistent with spectral measurements of Mg-rich olivine (Bates et al., 2020; Hamilton, 2010; Lane et al., 2011); near 9.35, 9.85, 10.75, 11.50, 19.74, 21.05, 24.26, 29.91, and 34.94  $\mu\text{m}$  (Table 3).

In the stage II and stage IV emissivity spectra measured under SAE conditions, we observe a shift of the CF to shorter wavelengths (of up to 0.21  $\mu\text{m}$ ) relative to measurements under ambient conditions, consistent with previous observations of anhydrous physical mixtures and anhydrous meteorites under SAE conditions (Donaldson Hanna et al., 2019), but opposite to what is observed in the aqueously altered CM spectra, where the CF shifts to longer wavelengths under SAE conditions. The spectral contrast of some vibrational features in the EET 96029 and Y 793321 spectra are reduced under SAE, although their positions do not change. The one exception is the 9.35  $\mu\text{m}$  feature in the EET 96029 spectrum, which shifts to shorter wavelengths (near 9.17  $\mu\text{m}$ ) under SAE conditions. Additionally, in the EET 96029 spectrum, a vibrational feature near 11.50  $\mu\text{m}$  becomes more distinct.

### 3.4. Aqueously and Thermally Altered CM-Anomalous Chondrites

#### 3.4.1. NIR Reflectance Spectral Features

Figure 4a shows the 3  $\mu\text{m}$  feature for the stage II CM-an WIS 91600. It shows a sharp feature near 2.72  $\mu\text{m}$ , and a broader feature near 2.90  $\mu\text{m}$ , which is similar in shape to the 3  $\mu\text{m}$  features observed in CI1 chondrites (Bates et al., 2020; Hiroi & Pieters, 1996; Takir et al., 2013). The observed spectral shape is consistent in position with the features observed in smectite phyllosilicate standard spectra (e.g., Bates et al., 2020; Salisbury et al., 1991), with the 2.72  $\mu\text{m}$  feature due to Mg-OH and the 2.90  $\mu\text{m}$  due to interlayer H<sub>2</sub>O. This is consistent with reports of mixed serpentine and smectite phyllosilicates in WIS 91600 (Lipschutz et al., 1999; Tonui et al., 2014).

#### 3.4.2. Ambient and SAE MIR Spectral Features

Figure 4b shows the ambient and SAE emissivity spectra of the stage II CM-an WIS 91600. The ambient emissivity spectrum shows a strong emissivity feature between 5 and 8, with two peaks at 6.61 and 6.90  $\mu\text{m}$ . A vibrational feature at 9.81  $\mu\text{m}$  is likely due to phyllosilicates, some of which are only partially dehydrated in WIS 91600. WIS 91600 also contains 12 vol% olivine, resulting in a feature at 10.69  $\mu\text{m}$ . In the Si-O bending region, the ambient spectrum shows features at 24.36 and 34.96  $\mu\text{m}$  that are consistent with Mg-rich

olivine (Hamilton, 2010; Lane et al., 2011), although features diagnostic of Mg-rich olivine near 19.75 and 21.05  $\mu\text{m}$  are absent. There is a feature at 29.47  $\mu\text{m}$  that is consistent with olivine, however WIS 91600 contains significant magnetite ( $\sim 9$  vol%, Table 1), which also has a feature at that position (Christensen et al., 2000). Thus, we cannot uniquely determine the mineral phase that causes this feature.

Under SAE conditions, the main changes in the emissivity spectrum of WIS 91600 occur in the region around the CF. The vibrational feature at 9.81  $\mu\text{m}$  is no longer resolvable, moving the CF to a longer wavelength at 9.32  $\mu\text{m}$ . Between 5 and 8  $\mu\text{m}$ , there is a change in spectral slope, which shifts the initial vibrational feature from 6.61 to 6.48  $\mu\text{m}$ . Across the rest of the spectral range, other vibrational features do not change in position.

### 3.5. Aqueously and Thermally Altered CY Chondrites

#### 3.5.1. NIR Reflectance Spectral Features

Figures 5a and 5b show the 3  $\mu\text{m}$  features for the CY chondrite spectra. The stage III spectrum shows a feature near 2.89  $\mu\text{m}$ , and stage IV CY spectra show a feature near 2.91  $\mu\text{m}$  (Table 2). The band area of these features does not change significantly either, from  $0.07 \pm 0.01 \mu\text{m}^{-1}$  to  $\sim 0.05 \pm 0.01 \mu\text{m}^{-1}$ . As these parameters are both within error of each other, there is no resolvable change of the 3  $\mu\text{m}$  feature with increasing thermal alteration in the CY spectra (Table 2).

#### 3.5.2. Ambient and SAE MIR Spectral Features

The ambient and SAE spectra of the stage III and stage IV CY chondrites are shown in Figures 5c and 5d. The ambient emissivity spectrum of Y 980115 shows a strong emissivity feature between 5 and 8  $\mu\text{m}$ , with two peaks at 6.54 and 6.93  $\mu\text{m}$  (Figure 5c). This may be due to carbonates in Y 980115. The ambient spectra of the stage IV CY chondrites have weaker features between 5 and 8  $\mu\text{m}$  (Figure 5d), meaning that this region can therefore be used to distinguish between stage III and stage IV CY spectra.

The Y 980115 ambient emissivity spectrum has a CF near 9.03  $\mu\text{m}$  and a TF at 12.61  $\mu\text{m}$ . Spectral contrast in the Si-O stretching and bending vibrational regions in the Y 980115 ambient spectrum is lower than that observed for the CM ambient spectra and few diagnostic features are observed, except for a feature at 9.85  $\mu\text{m}$ . Based on the shape of this feature, we suggest that it is due to Si-O stretching in dehydrated phyllosilicates. We observe weak features at wavelengths  $>20 \mu\text{m}$ , although their spectral contrast is low, likely due to the high abundance of Fe-sulfides (Table 1). Fe-sulfides have low albedo and can act as an opaque agent, reducing the strength of vibrational features and overall spectral contrast (Cloutis et al., 2011). Features near 25.72 and 35.85  $\mu\text{m}$  are also identified and are consistent with  $\sim\text{Fo}\#60$  olivine (Hamilton, 2010; Lane et al., 2011).

The region around the CF in the stage IV CY emissivity spectra is complex and identifying the CF position is challenging. The Y 86720 and Y 86789 ambient emissivity spectra show a shoulder near 8.35  $\mu\text{m}$  that is consistent with the CF of pyroxene (Hamilton, 2000). These meteorites contain 8 and 5 vol% pyroxene, respectively (Table 1). The 8.35  $\mu\text{m}$  feature is followed by another emissivity peak near 9.00  $\mu\text{m}$ . This 9  $\mu\text{m}$  feature is in a similar position to the CF in the Y 980115 spectrum, but rather than being related to dehydrated phyllosilicates, which are not present in the stage IV CYs (Table 1), it likely represents olivine: its position is consistent with the CF in Fo60-Fo80 olivine (Hamilton, 2010), and the samples contain  $\sim 60$  vol% secondary olivine (Table 1). There is a TF near 12.60  $\mu\text{m}$  in both stage IV CY spectra. The Y 86720 and Y 86789 ambient spectra also show vibrational features near 9.81, 10.35, 11.78, 20.19, 25.48, 30.83, and 35.95  $\mu\text{m}$ , which are consistent with more Fe-rich olivine ( $\sim\text{Fo}60\text{--}\text{Fo}70$ , Hamilton, 2010).

The B 7904 ambient emissivity spectrum shows a shoulder at 8.48  $\mu\text{m}$ , consistent with the CF of some pyroxenes (Donaldson Hanna, Wyatt, et al., 2012; Hamilton, 2000), and then a CF at 9.27. The spectrum has a transparency feature at 12.61  $\mu\text{m}$ . The B 7904 spectrum shows vibrational features in the Si-O stretching region at 9.73 and 10.72  $\mu\text{m}$ . These are in similar positions to the olivine vibrational features identified in the stage II and stage IV CM ambient emissivity spectra. However, the Si-O bending region of B 7904 resembles the other stage IV CY spectra, with features consistent with recrystallized, Fe-rich olivine at 20.12, 25.49, 30.61, and 36.01  $\mu\text{m}$ . B 7904 contains both  $\sim 25$  vol% primary, Mg-rich olivine, and  $\sim 50$  vol% secondary olivine (Table 1).

**Table 3**

*The Midinfrared (MIR) Spectral Parameters Determined Under (a) Ambient and (b) Simulated Asteroid Environment (SAE) Conditions. Included in Italics are the*

Meteorite	Classification	Heating Stage	6 $\mu\text{m}$ features ( $\mu\text{m}$ )			Christiansen feature ( $\mu\text{m}$ )	
ALH 83100	CM1/2	-	6.16 $\pm$ 0.01	6.96 $\pm$ 0.01	7.23 $\pm$ 0.01	9.05 $\pm$ 0.03	-
ALH 83102	CM2	-	6.16 $\pm$ 0.01	6.97 $\pm$ 0.01	7.25 $\pm$ 0.01	9.06 $\pm$ 0.02	-
LON 94101	CM2	-	6.17 $\pm$ 0.01	6.94 $\pm$ 0.01	7.24 $\pm$ 0.01	9.01 $\pm$ 0.03	-
Murchison	CM2	-	6.17 $\pm$ 0.02	-	7.17 $\pm$ 0.01	8.78 $\pm$ 0.01	9.29 $\pm$ 0.01
EET 96029	CM2	2	6.10 $\pm$ 0.01	-	-	8.86 $\pm$ 0.02	9.38 $\pm$ 0.02
Y 793321	CM2	2	6.17 $\pm$ 0.01	-	-	8.89 $\pm$ 0.03	9.34 $\pm$ 0.02
PCA 02010	CM2	4	6.10 $\pm$ 0.01	-	-	8.75 $\pm$ 0.01	9.40 $\pm$ 0.01
PCA 02012	CM2	4	6.09 $\pm$ 0.01	-	-	8.47 $\pm$ 0.05	9.39 $\pm$ 0.01
WIS 91600	CM-an	2	-	6.61 $\pm$ 1	6.90 $\pm$ 0.02	9.04 $\pm$ 0.01	-
Y 980115	CI1/CY	3	-	6.54 $\pm$ 0.02	6.93 $\pm$ 0.02	9.03 $\pm$ 0.02	-
B 7904	C2-ung/CY	4	-	-	-	9.27 $\pm$ 0.02	-
Y 86720	C2-ung/CY	4	-	-	-	8.99 $\pm$ 0.01	9.82 $\pm$ 0.01
Y 86789	C2-ung/CY	4	6.14 $\pm$ 0.01	-	-	9.02 $\pm$ 0.01	9.80 $\pm$ 0.02
Meteorite	Classification	Heating Stage	6 $\mu\text{m}$ features ( $\mu\text{m}$ )			Christiansen feature ( $\mu\text{m}$ )	
ALH 83100	CM2	-	6.20 $\pm$ 0.01	6.89 $\pm$ 0.01	7.23 $\pm$ 0.01	9.17 $\pm$ 0.01	-
ALH 83102	CM2	-	6.17 $\pm$ 0.01	6.86 $\pm$ 0.01	7.21 $\pm$ 0.01	9.10 $\pm$ 0.01	-
LON 94101	CM2	-	6.24 $\pm$ 0.02	6.86 $\pm$ 0.01	7.20 $\pm$ 0.01	9.16 $\pm$ 0.01	-
Murchison	CM2	-	6.16 $\pm$ 0.01	-	7.18 $\pm$ 0.01	8.71 $\pm$ 0.01	9.34 $\pm$ 0.01
EET 96029	CM2	2	6.05 $\pm$ 0.02	-	-	8.65 $\pm$ 0.02	9.16 $\pm$ 0.03
Y 793321	CM2	2	6.12 $\pm$ 0.02	-	-	8.84 $\pm$ 0.02	-
PCA 02010	CM2	4	6.08 $\pm$ 0.01	-	-	8.59 $\pm$ 0.01	9.38 $\pm$ 0.01
PCA 02012	CM2	4	6.09 $\pm$ 0.01	-	-	8.52 $\pm$ 0.01	9.41 $\pm$ 0.01
WIS 91600	CM-an	2	-	6.48 $\pm$ 0.02	6.93 $\pm$ 0.02	9.32 $\pm$ 0.01	-
Y 980115	CI1/CY	3	-	6.42 $\pm$ 0.01	6.96 $\pm$ 0.01	9.23 $\pm$ 0.02	-
B 7904	C2-ung/CY	4	6.26 $\pm$ 0.01	-	-	9.23 $\pm$ 0.01	-
Y 86720	C2-ung/CY	4	6.36 $\pm$ 0.03	-	-	9.39 $\pm$ 0.06	-
Y 86789	C2-ung/CY	4	6.12 $\pm$ 0.01	-	-	9.59 $\pm$ 0.07	-

Abbreviations: ALH, Alan Hills; EET, Elephant Moraine; LON, Lonewulf Nunataks; PCA, Pecora Escarpment; WIS, Wisconsin Range.

Under SAE conditions, the CF in the Y 980115 spectrum shifts to slightly lower wavelengths, and the vibrational feature at 9.35  $\mu\text{m}$  is no longer identifiable. The spectral contrast in the Si-O bending range is reduced relative to the ambient emissivity spectrum. In the stage IV Y 86720 and Y 86789 spectra under SAE conditions, the feature near 9.81  $\mu\text{m}$  is no longer distinguishable, causing the peak at 9.00  $\mu\text{m}$  to shift to longer wavelengths for Y 86720 (9.39  $\mu\text{m}$ ) and Y 86789 (9.59  $\mu\text{m}$ ). The B 7904 emissivity spectrum shows little change in the CF region under SAE conditions, with the feature at 9.73  $\mu\text{m}$  still resolvable and no shift in the CF position. In the Si-O bending region, the SAE spectral signature of all stage IV CYs appears smoother, in contrast to the more complex ambient spectra. However, the positions of the vibrational features do not change under SAE conditions.

*Spectral Parameters Determined for the Ambient and SAE Emissivity Spectra of the CM2 Murchison Collected by Donaldson Hanna et al. (2021)*

Si-O stretching features ( $\mu\text{m}$ )			Transparency feature ( $\mu\text{m}$ )			Si-O bending features ( $\mu\text{m}$ )		
9.83 $\pm$ 0.01	-	-	11.56 $\pm$ 0.01	-	-	23.32 $\pm$ 0.05	31.29 $\pm$ 0.08	36.35 $\pm$ 0.14
9.83 $\pm$ 0.01	-	-	11.54 $\pm$ 0.01	-	-	23.22 $\pm$ 0.03	31.23 $\pm$ 0.02	36.95 $\pm$ 0.06
9.82 $\pm$ 0.01	-	-	11.30 $\pm$ 0.01, 12.32 $\pm$ 0.01	-	-	23.76 $\pm$ 0.04	31.15 $\pm$ 0.04	38.00 $\pm$ 0.08
9.90 $\pm$ 0.01	-	-	11.40 $\pm$ 0.01, 12.22 $\pm$ 0.01	19.72 $\pm$ 0.05	21.07 $\pm$ 0.01	24.05 $\pm$ 0.03	-	34.99 $\pm$ 0.01
9.84 $\pm$ 0.01	10.65 $\pm$ 0.01	-	12.47 $\pm$ 0.01	19.81 $\pm$ 0.06	21.17 $\pm$ 0.01	24.10 $\pm$ 0.01	29.79 $\pm$ 0.01	34.86 $\pm$ 0.03
9.88 $\pm$ 0.01	10.65 $\pm$ 0.01	-	12.54 $\pm$ 0.02	19.59 $\pm$ 0.01	21.05 $\pm$ 0.01	23.98 $\pm$ 0.01	29.96 $\pm$ 0.01	35.05 $\pm$ 0.03
9.85 $\pm$ 0.01	10.66 $\pm$ 0.03	11.77 $\pm$ 0.01	12.45 $\pm$ 0.03	19.79 $\pm$ 0.01	20.97 $\pm$ 0.02	24.72 $\pm$ 0.02	30.04 $\pm$ 0.03	35.02 $\pm$ 0.02
9.88 $\pm$ 0.01	10.62 $\pm$ 0.03	11.77 $\pm$ 0.01	12.50 $\pm$ 0.01	19.76 $\pm$ 0.03	21.00 $\pm$ 0.01	24.25 $\pm$ 0.01	29.86 $\pm$ 0.03	34.84 $\pm$ 0.02
9.81 $\pm$ 0.01	10.69 $\pm$ 0.01	-	12.53 $\pm$ 0.01	-	-	24.36 $\pm$ 0.12	29.47 $\pm$ 0.15	38.50 $\pm$ 0.03
9.85 $\pm$ 0.02	-	-	12.61 $\pm$ 0.04	-	-	25.72 $\pm$ 0.01	-	35.85 $\pm$ 0.05
9.73 $\pm$ 0.02	10.72 $\pm$ 0.01	11.75 $\pm$ 0.01	12.61 $\pm$ 0.01	20.12 $\pm$ 0.16	-	25.49 $\pm$ 0.01	30.61 $\pm$ 0.03	36.01 $\pm$ 0.05
10.33 $\pm$ 0.01	-	11.78 $\pm$ 0.01	12.61 $\pm$ 0.01	20.15 $\pm$ 0.07	-	25.41 $\pm$ 0.02	30.87 $\pm$ 0.01	35.71 $\pm$ 0.04
10.36 $\pm$ 0.01	-	11.77 $\pm$ 0.01	12.63 $\pm$ 0.02	20.23 $\pm$ 0.06	-	25.55 $\pm$ 0.03	30.79 $\pm$ 0.01	36.18 $\pm$ 0.05
Si-O stretching features ( $\mu\text{m}$ )			Transparency feature ( $\mu\text{m}$ )			Si-O bending features ( $\mu\text{m}$ )		
9.84 $\pm$ 0.04	-	-	11.49 $\pm$ 0.01	-	-	23.28 $\pm$ 0.05	31.98 $\pm$ 0.04	36.62 $\pm$ 0.06
9.86 $\pm$ 0.06	-	-	11.43 $\pm$ 0.01	-	-	23.31 $\pm$ 0.03	32.30 $\pm$ 0.01	37.61 $\pm$ 0.03
9.84 $\pm$ 0.04	-	-	11.39 $\pm$ 0.01, 12.34 $\pm$ 0.04	-	-	23.73 $\pm$ 0.04	30.73 $\pm$ 0.03	37.98 $\pm$ 0.07
9.88 $\pm$ 0.03	-	-	11.46 $\pm$ 0.03, 12.26 $\pm$ 0.01	19.74 $\pm$ 0.05	21.25 $\pm$ 0.01	24.00 $\pm$ 0.02	-	35.06 $\pm$ 0.03
-	10.87 $\pm$ 0.03	11.49 $\pm$ 0.01	12.51 $\pm$ 0.03	19.80 $\pm$ 0.04	21.05 $\pm$ 0.01	24.11 $\pm$ 0.01	30.06 $\pm$ 0.06	35.06 $\pm$ 0.03
-	-	11.62 $\pm$ 0.01	12.60 $\pm$ 0.01	19.76 $\pm$ 0.05	21.00 $\pm$ 0.01	24.03 $\pm$ 0.02	30.22 $\pm$ 0.05	34.97 $\pm$ 0.03
9.95 $\pm$ 0.01	10.83 $\pm$ 0.03	11.69 $\pm$ 0.01	12.39 $\pm$ 0.03	19.77 $\pm$ 0.05	20.97 $\pm$ 0.01	24.47 $\pm$ 0.04	30.13 $\pm$ 0.05	-
9.94 $\pm$ 0.02	10.77 $\pm$ 0.03	11.78 $\pm$ 0.01	12.51 $\pm$ 0.03	19.83 $\pm$ 0.02	20.97 $\pm$ 0.01	24.15 $\pm$ 0.03	30.32 $\pm$ 0.09	-
-	10.74 $\pm$ 0.02	-	12.53 $\pm$ 0.02	-	-	24.39 $\pm$ 0.08	29.54 $\pm$ 0.02	35.02 $\pm$ 0.05
-	-	-	12.52 $\pm$ 0.01	-	-	-	-	-
9.63 $\pm$ 0.01	10.58 $\pm$ 0.02	11.83 $\pm$ 0.01	12.68 $\pm$ 0.03	20.10 $\pm$ 0.01	-	25.48 $\pm$ 0.05	30.78 $\pm$ 0.05	-
10.43 $\pm$ 0.01	-	11.76 $\pm$ 0.01	12.58 $\pm$ 0.03	20.46 $\pm$ 0.02	-	25.45 $\pm$ 0.03	30.89 $\pm$ 0.03	-
10.44 $\pm$ 0.01	-	11.77 $\pm$ 0.01	12.60 $\pm$ 0.05	20.39 $\pm$ 0.02	-	25.49 $\pm$ 0.03	30.80 $\pm$ 0.03	-

## 4. Discussion

### 4.1. Near Infrared Spectral Relationships With Mineralogy

The 3  $\mu\text{m}$  absorption is caused by the stretching, bending and overtone vibrations of  $\text{H}_2\text{O}$  and the stretching vibration of  $-\text{OH}$ . Water causes features near 3.1  $\mu\text{m}$ , whereas the position of the feature caused by the  $-\text{OH}$  tend to be between 2.5 and 3.0  $\mu\text{m}$  depending on the cations to which those molecules are bound (Gaffey et al., 1993). Studies of the 3  $\mu\text{m}$  region in CM and CI chondrite spectra show a correlation between the position of the feature and the mineralogy of the meteorite, with features shifting to shorter wavelengths as the abundance of Mg-serpentine increases with the degree of alteration (Bates et al., 2020; Beck et al., 2010;



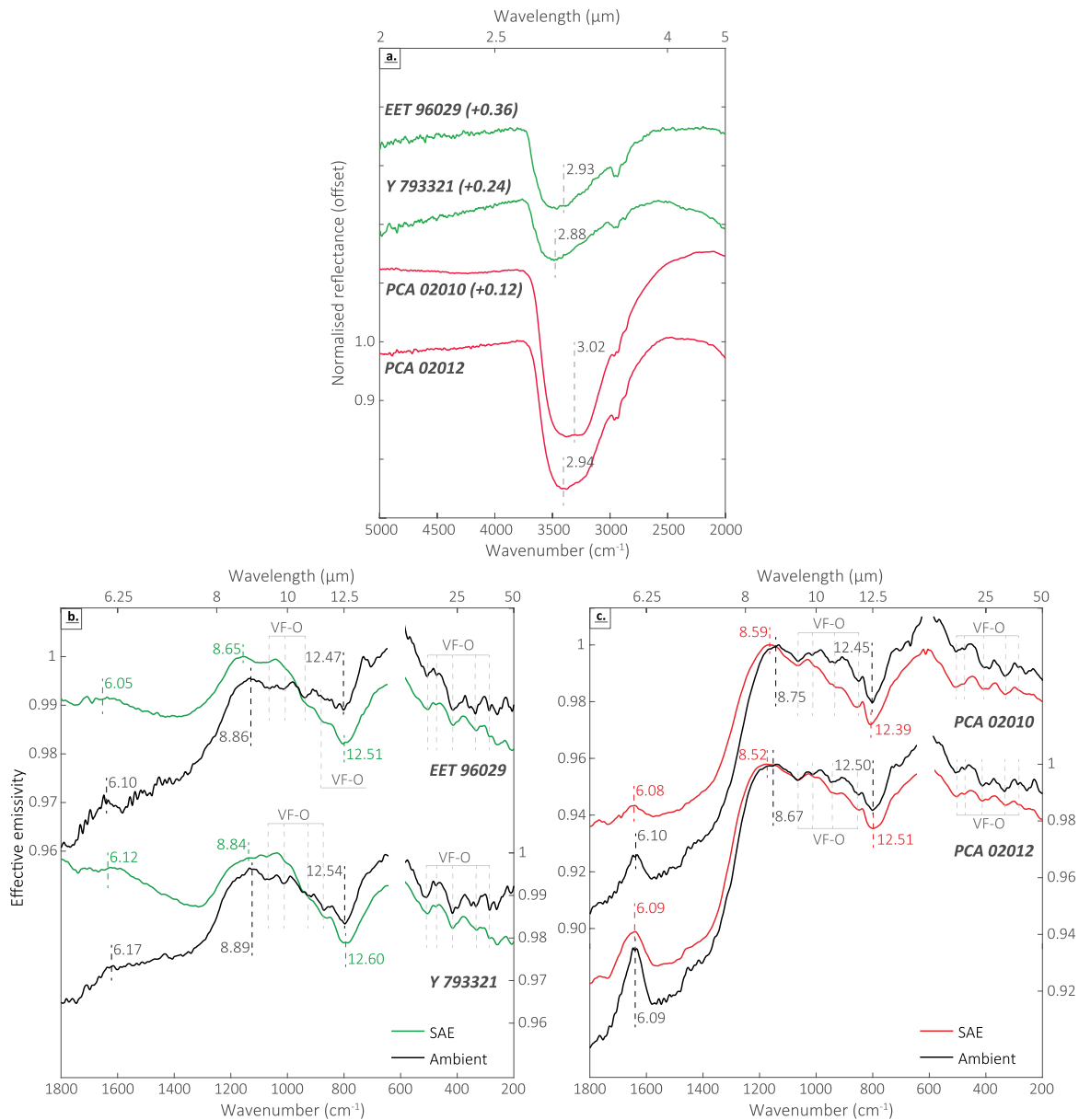


**Figure 3.** (a) The near-infrared (NIR) reflectance spectra between 2 and 5  $\mu\text{m}$  for the stage II CMs Elephant Moraine (EET) 96029 and Y 793321 and the stage IV CMs Pecora Escarpment (PCA) 02010 and PCA 02012. Spectra are normalized to a linear continuum fitted to points on either side of the feature (2.65–3.87  $\mu\text{m}$ ) and offset by the value given in brackets next to the meteorite name. (b) The midinfrared (MIR) emissivity spectra between 5.5 and 50  $\mu\text{m}$  for EET 96029 and Y 793321 collected under ambient (black) and simulated asteroid environment (SAE) (green) conditions. (c) The MIR emissivity spectra between 5.5 and 50  $\mu\text{m}$  for PCA 02010 and PCA 02012 collected under ambient (black) and SAE (red) conditions. VF-P refers to vibrational features associated with phyllosilicates, and VF-O refers to vibrational features associated with olivine. Gaps in the spectra are a region of low signal to noise due to low beam splitter throughput.

Hanna et al., 2020; Takir et al., 2013). The 3  $\mu\text{m}$  features in the aqueously altered CM sample spectra in this study are consistent with this interpretation. Both ALH 83100 and ALH 83102 contain  $\sim 65$  vol% Mg-serpentine and their spectra have 3  $\mu\text{m}$  features with sharp minima near 2.72  $\mu\text{m}$ . The LON 94101 spectrum shows two features in this region, at 2.72 and 2.80  $\mu\text{m}$ , the former consistent with more Mg-serpentine phyllosilicate and the latter with Fe-cronstedtite. Takir et al. (2013) suggested that this spectral shape reflects an intermediate composition between the more aqueously altered meteorite spectra with features at shorter wavelengths and the less altered meteorite spectra with features at longer wavelengths. LON 94101 does

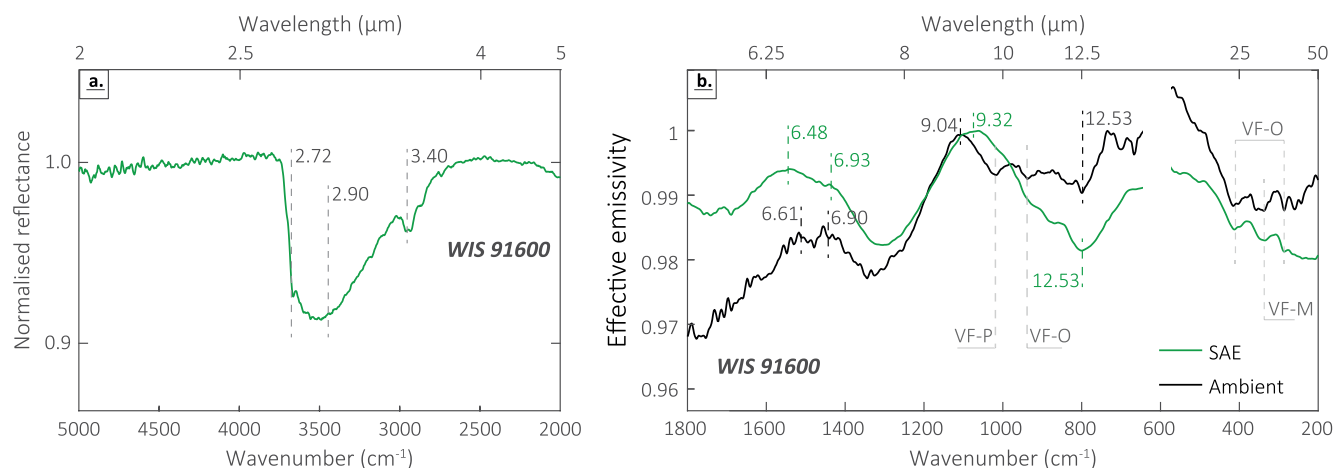


**Figure 4.** (a) The near-infrared (NIR) reflectance spectra between 2 and 5  $\mu\text{m}$  for the stage II CM-an Wisconsin Range (WIS) 91600. Spectra are normalized to a linear continuum fitted to points on either side of the feature (2.65–3.87  $\mu\text{m}$ ). (b) The MIR emissivity spectra between 5.5 and 50  $\mu\text{m}$  for WIS 91600 collected under ambient (black) and simulated asteroid environment (SAE) (green) conditions. VF-P refers to vibrational features associated with phyllosilicates, VF-O refers to vibrational features associated with olivine and VF-M refers the potential magnetite vibrational feature. Gaps in the spectra are a region of low signal to noise due to low beam splitter throughput.

contain a slightly higher abundance of Fe-cronstedtite in comparison to the ALH 83100 and ALH 83102 samples (22 vol% compared to ~19 vol%), potentially explaining the “intermediate” feature.

All thermally altered CM, CM-an, and CY spectra show a 3  $\mu\text{m}$  feature. As spectra were collected on samples that had been heated to drive off adsorbed terrestrial water, the presence of a 3  $\mu\text{m}$  feature indicates that a -OH/H<sub>2</sub>O component remains in these meteorites despite their thermal histories. Typically, the 3  $\mu\text{m}$  features in the stage II, III, and IV sample (regardless of meteorite type) spectra show features between 2.88 and 3.02  $\mu\text{m}$  (Figures 3a, 4a, 5a and 5b). Unlike the aqueously altered CM spectra, the positions of these features are not influenced by the degree of aqueous alteration: for example, the position and shape of the 3  $\mu\text{m}$  feature in the stage II spectra do not vary with disordered phyllosilicate abundance. Figure 6 shows that there is a significant shift in feature position between aqueously altered CM spectra and dehydrated CM spectra, however, there is not a convincing trend in position within the dehydrated CM spectra. This trend of the feature shifting to longer wavelengths with thermal alteration is consistent with previous measurements of thermally altered CM and CY chondrites (Hiroi et al., 1996, 1997). The difference between aqueously altered and dehydrated CM spectra is also demonstrated in the experimentally dehydrated Murchison spectra from Tonui et al. (2014), who showed that the Murchison spectrum has a 3  $\mu\text{m}$  feature near 2.80  $\mu\text{m}$ , but this shifts to 2.90  $\mu\text{m}$  upon thermal alteration to 400°C.

The stage IV CM spectra show features at 2.94 and 3.02  $\mu\text{m}$  (Figure 3a, Table 2), and they show larger band areas ( $\sim 0.16 \mu\text{m}^{-1}$ ) than in any other thermally altered spectra. This is consistent with previous spectral observations of PCA 02010, where the large band depth was attributed to the presence of rusts (Hanna et al., 2020). Rusts are very poorly crystalline, and are difficult to analyze using XRD; however, the TGA results of Garenne et al. (2014) showed a mass loss event at  $\sim 225^\circ\text{C}$  in both PCA 02010 and PCA 02012 (their Figure 11). This mass loss agrees with the dehydration of rusts (e.g., King et al., 2015, 2021) and is similar to a dehydration event reported at  $225^\circ\text{C}$  observed during TGA of the CM1 chondrites GRO 95645 and MIL 07689 which were observed to have anomalously large band areas (Bates et al., 2020). We suggest this phase may contribute to the increased band area observed for the 3  $\mu\text{m}$  features of PCA 02010 and PCA 02012.

The WIS 91600 spectrum has a 3  $\mu\text{m}$  feature that shares some similarities with the features observed in CI spectra (Bates et al., 2020; Hiroi & Pieters, 1996; Takir et al., 2013). As discussed above, this likely reflects Mg-rich serpentine and smectite in WIS 91600. The band area calculated for the WIS 91600 3  $\mu\text{m}$  feature ( $0.04 \mu\text{m}^{-1}$ ) is however smaller than those calculated for the CI spectra ( $0.22$  and  $0.23 \mu\text{m}^{-1}$ , Bates et al., 2020), and is instead more consistent with the areas measured in the stage II CM spectra (Table 2). Spectra of experimentally dehydrated Ivuna show a 3  $\mu\text{m}$  feature that remains at 2.72  $\mu\text{m}$  even at temperatures of  $600^\circ\text{C}$ ,

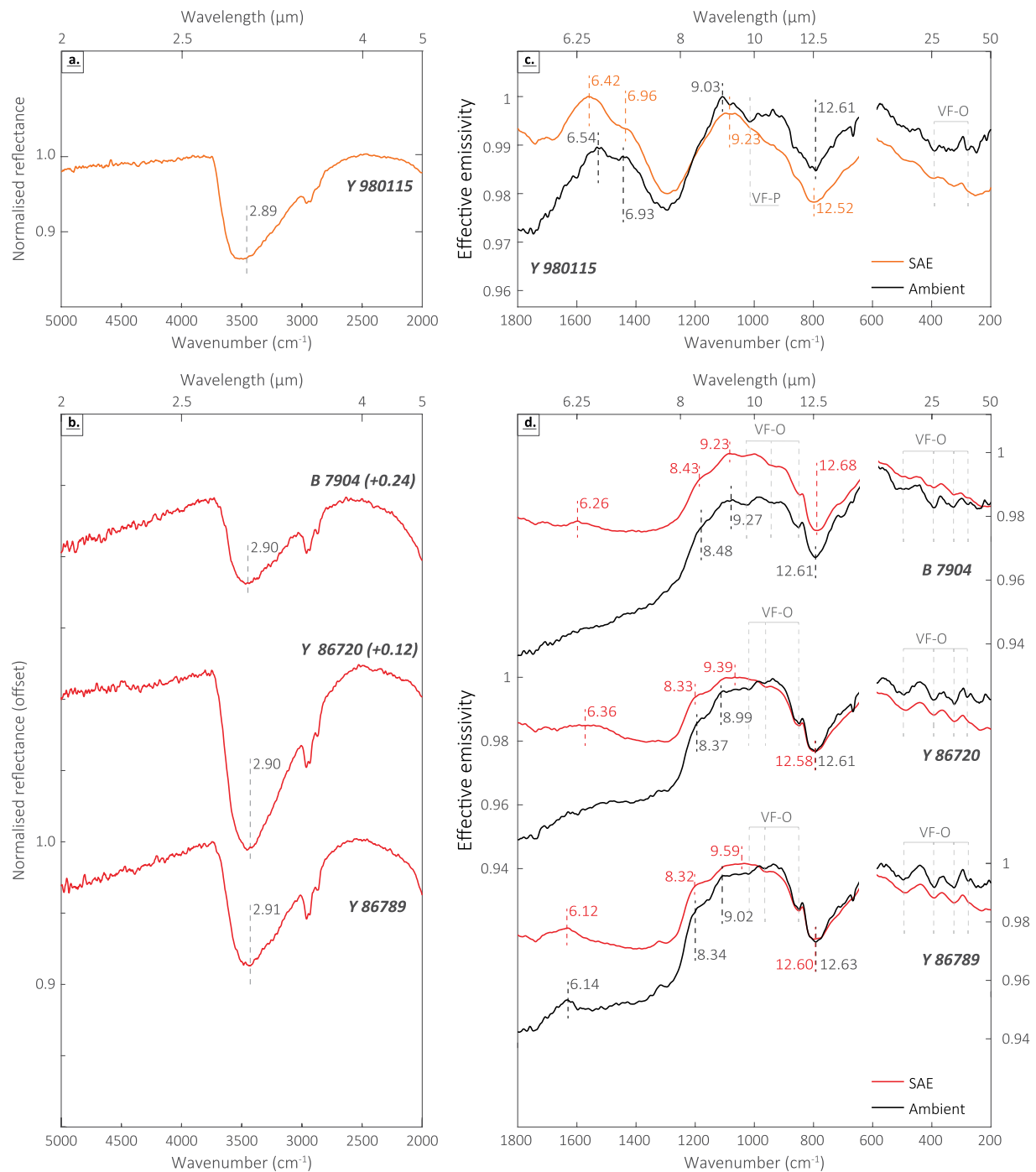


**Figure 5.** The near-infrared (NIR) reflectance spectra between 2 and 5  $\mu\text{m}$  for (a) the stage III CY Y 980115 and (b) the stage IV CYs B 7904, Y 86720, and Y 86789. Spectra are normalized to a linear continuum fitted to points on either side of the feature (2.65–3.87  $\mu\text{m}$ ) and offset by the value given in brackets next to the meteorite name. (b) The midinfrared (MIR) emissivity spectra between 5.5 and 50  $\mu\text{m}$  for (a) Y 980115, and (b) B 7904, Y 86720 and Y 86789 collected under ambient (black) and simulated asteroid environment (SAE) (orange/red) conditions. VF-P refers to vibrational features associated with phyllosilicates and VF-O refers to vibrational features associated with olivine. Gaps in the spectra are a region of low signal to noise due to low beam splitter throughput.

although the depth of the feature is reduced relative to the aqueously altered spectra (Hiroi & Pieters, 1996). This may be due to the smectite phyllosilicate component of the CI chondrite, with Alemanno et al. (2020) showing that the 3  $\mu\text{m}$  feature of saponite retains its sharp 2.72  $\mu\text{m}$  feature upon experimental heating to 700°C, whereas the 2.72  $\mu\text{m}$  feature in the spectra of serpentine samples becomes less distinct at similar

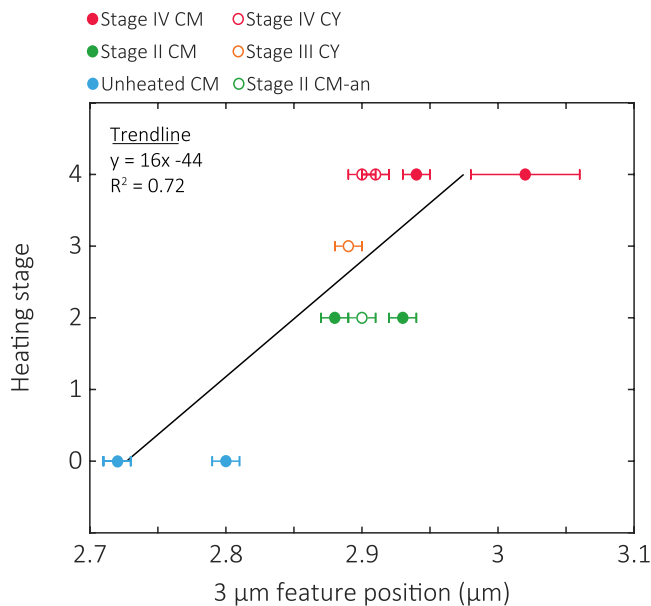


**Figure 6.** The position of the 3  $\mu\text{m}$  feature against heating stage. All aqueously altered samples are given the heating stage 0, and we plot both the 2.72 and 2.80  $\mu\text{m}$  features observed in the Lonewolf Nunataks (LON) 94101 spectra. With increasing metamorphic temperature, the position shifts to longer wavelengths.

temperatures. This is therefore further evidence that WIS 91600 contains dehydrated smectite phyllosilicates.

## 4.2. MIR Emissivity Spectra

### 4.2.1. Comparisons Between Ambient and SAE Emissivity Spectra

The effect of varying environmental conditions on MIR emissivity spectra has been discussed previously (e.g., Donaldson Hanna, Wyatt, et al., 2012; Donaldson Hanna, Thomas, et al., 2012, 2019, 2021; Henderson & Jakosky, 1994; Logan et al., 1973; Salisbury & Walter, 1989; Thomas et al., 2010). However, in this study, we show variable changes when measuring under ambient and SAE conditions depending on the petrologic type and alteration history of the meteorite. One key parameter is the CF, which in CM chondrites appears to shift to longer wavelengths under SAE conditions for the aqueously altered CM chondrite spectra (Figure 2), and to shorter wavelengths under SAE for the thermally altered CM chondrite spectra (Figure 3).

Typically, introduction of a thermal gradient results in a shift in the CF to shorter wavelengths as a result of the different temperatures between the CF region (where radiation is emitted from the relatively warm interior due to little scattering as it passes through the material) and the vibrational features (where radiation from the relatively cool shallower layers is emitted, due to most materials having high absorption coefficients in these wavelength ranges) (e.g., Donaldson Hanna, Wyatt, et al., 2012; Donaldson Hanna, Thomas, et al., 2012; Donaldson Hanna et al., 2019; Henderson & Jakosky, 1994; Logan et al., 1973; Salisbury & Walter, 1989; Thomas et al., 2010). This is the phenomenon we observed in the thermally altered CM spectra when comparing spectra collected under ambient and SAE conditions. The opposite behavior in the aqueously altered CM chondrite spectra may be due to the method of calibration when reducing the spectra to emissivity. During this process, a single brightness temperature of the sample is assumed, when in reality several temperatures at varying depths are being detected by the spectrometer. This may cause spectral slopes to appear in the CF region of spectra, which are not a result of the mineralogy of the sample. In the spectra of ALH 83100, ALH 83102, and LON 94101 it appears as though the shift in the CF position to longer wavelengths in the SAE spectra could be a result of a change in spectral slope. Therefore, the variability in reactions to being measured under SAE conditions may not be a result of changes in mineralogy.

In contrast to the CM chondrite spectra, the shifts in CFs between ambient and SAE spectra of the CM-an and CY spectra seem to be a result of vibrational features appearing and disappearing. This is responsible for the shift in the CF in the WIS 91600, Y 980115, Y 86720 and Y 86789 spectra. One hypothesis is that with the introduction of the thermal gradient in the samples under SAE conditions, different minerals are sampled owing to their optical properties in the resulting emissivity spectrum. Disappearance of features characteristic of certain minerals certainly suggests they are no longer emitting in the same way as they did under ambient conditions. Therefore, the difference between ambient and SAE spectra in the CYs compared the difference between ambient and SAE spectra in the CMs does appear to be a result of the differing mineralogy and therefore different alteration history. This could be explored by further investigating the optical properties of the minerals responsible for the appearing and disappearing features. The inconsistency in spectral changes when measuring under ambient and SAE conditions highlights the importance of measuring under the appropriate conditions.

### 4.2.2. Aqueous Alteration in MIR Emissivity Spectra

McAdam et al. (2015) and Bates et al. (2020) identified several trends in MIR reflectance spectra of CM chondrites, including shifts of the CF and TF to shorter wavelengths with increasing aqueous alteration. However, the CM2 chondrites in this work do not cover the same petrologic range as the samples analyzed

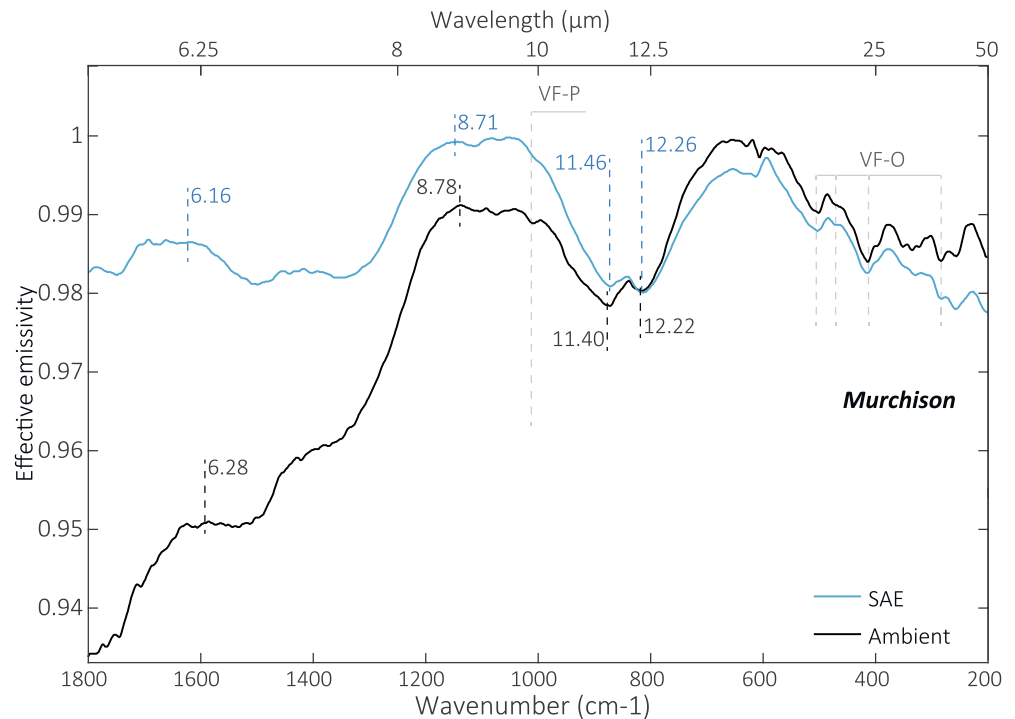


**Figure 7.** The midinfrared (MIR) emissivity spectra between 5.5 and 50  $\mu\text{m}$  for the CM2 Murchison from Donaldson Hanna et al. (2021), collected under ambient (black) and simulated asteroid environment (SAE) (blue) conditions. VF-P refers to vibrational features associated with phyllosilicates, VF-O refers to vibrational features associated with olivine and VF-M refers the potential magnetite vibrational feature. Gaps in the spectra are a region of low signal to noise due to a beam splitter error.

by Bates et al. (2020). To compensate for this, Figure 7 shows the ambient and SAE spectra of the CM chondrite Murchison (Donaldson Hanna et al., 2021), which has a PSF petrologic type of 1.5 and is less aqueously altered than ALH 83100, ALH 83102, and LON 94101 (Howard et al., 2015; Lindgren et al., 2011; Rubin et al., 2007; Zolensky et al., 1997). The Murchison sample shown in Figure 7, while still spectrally dominated by the finest particulate fraction, had a range of particle sizes (Donaldson Hanna et al., 2021), and therefore only first order comparisons can be made with spectra in this work which were collected from samples with particle sizes  $<35 \mu\text{m}$ . Nevertheless, comparison of the emissivity spectra for ALH 83100, ALH 83102, and LON 94101 (Figure 2b) to the spectra of Murchison (Figure 7), demonstrates that several of the trends used to evaluate aqueous alteration from reflectance spectra are also applicable to emissivity spectra. For example, the Murchison and LON 94101 spectra have doublet TF, while ALH 83100 and ALH 83102 emissivity spectra have a single feature at shorter wavelengths, which is consistent with ALH 83100 and ALH 83102 being more aqueously altered than Murchison and LON 94101 (Bates et al., 2020; McAdam et al., 2015). Additionally, the CF changes shape from a relatively broad feature in the Murchison spectra to a sharper feature in the LON 94101, ALH 83100, and ALH 83102 spectra, in agreement with Murchison being the least aqueously altered of these meteorites (Bates et al., 2020; McAdam et al., 2015).

The CF shifts to longer wavelengths in the more aqueously altered spectra, which is inconsistent with previous observations of powdered meteorite reflectance spectra (Bates et al., 2020), but has been reported for reflectance spectra collected from polished sections of CM chondrites (Hanna et al., 2020). In the ambient emissivity spectra, Murchison has a CF at  $8.78 \mu\text{m}$ , but the more altered ALH 83100, ALH 83102, and LON 94101 have CFs near  $9.01\text{--}9.05 \mu\text{m}$ . This may be due to the higher signal to noise of these emissivity spectra in comparison to reflectance measurements presented in Bates et al. (2020), allowing the CF to be clearly identified. In the reflectance spectrum of Murchison in Bates et al. (2020), the CF was identified as the center of a broad zone, whereas in the emissivity spectrum presented here, vibrational features can be more clearly identified, resulting in the CF being more distinguishable.



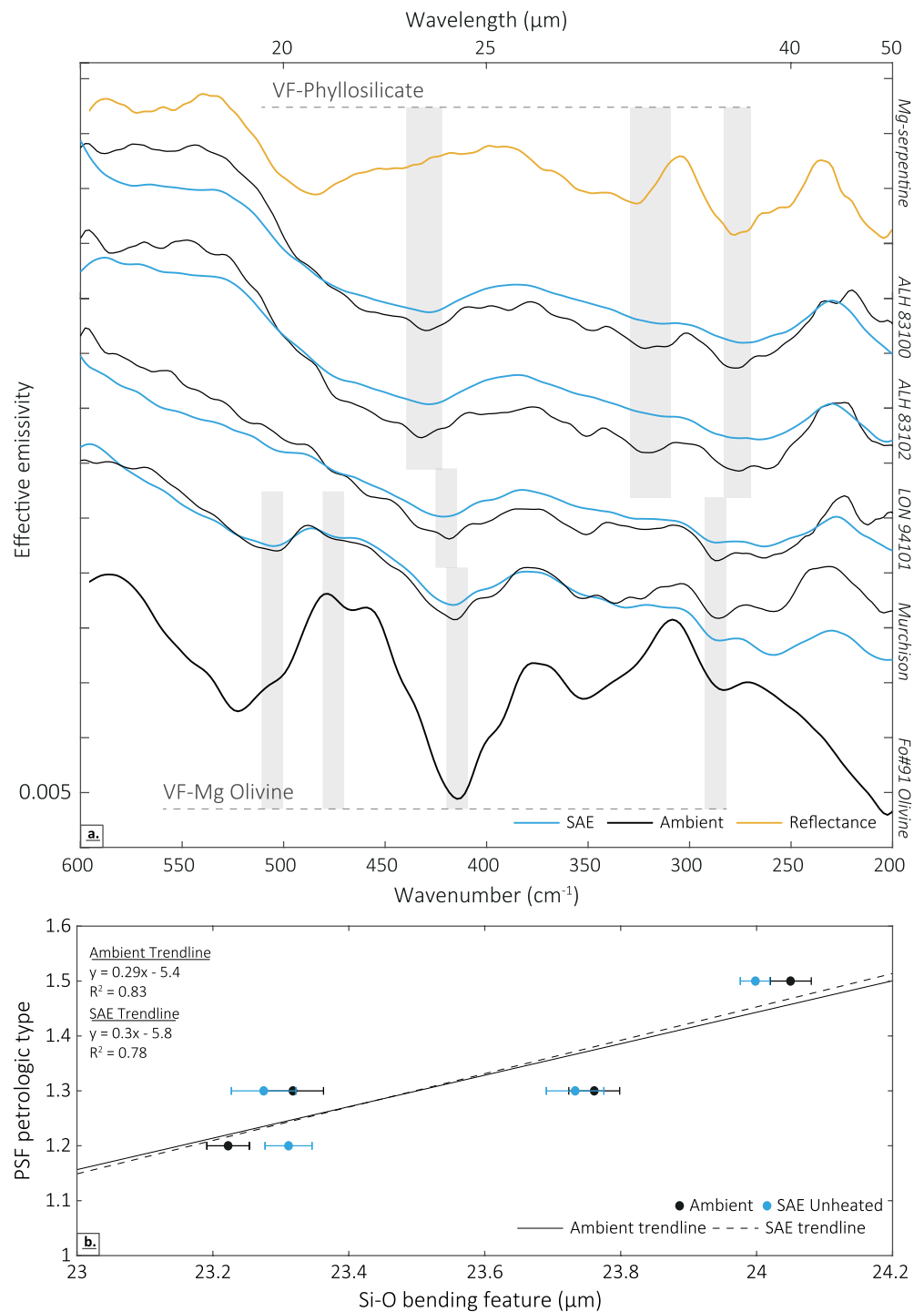


**Figure 8.** (a) The Si-O bending region, between 16.7 and 50  $\mu\text{m}$ , from the emissivity spectra of the unheated CMs in this study. The Murchison emissivity spectra are also included (Donaldson Hanna et al., 2021). Ambient (black) and simulated asteroid environment (SAE) (blue) spectra are offset, so they plot on top of each other for the same meteorite. The ambient spectrum of San Carlos Olivine (Fo91) and the reflectance spectrum of the Mg-rich serpentine lizardite from Bates et al. (2020) are also included for comparison. VF indicates vibrational features, and the reflectance spectra is plotted here as 1-reflectance so as to be comparable to the emissivity spectra. (b) The position of the Si-O bend feature between 23 and 26  $\mu\text{m}$  against petrologic type as determined by position-sensitive-detector X-ray diffraction (PSD-XRD).

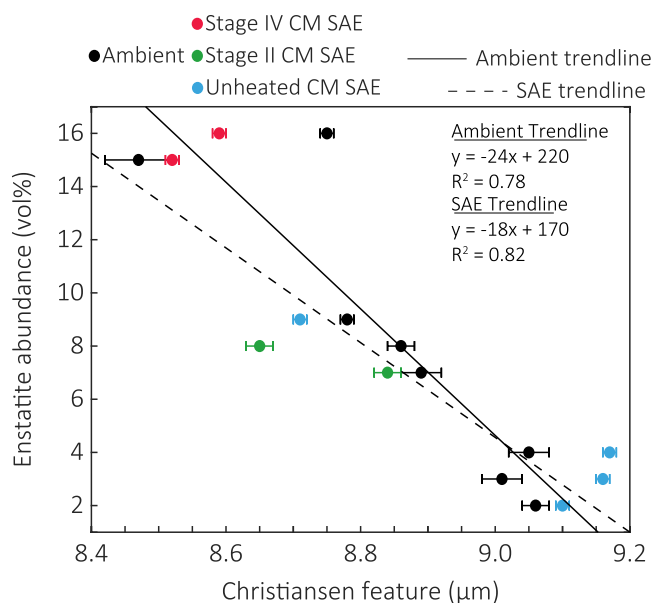


**Figure 9.** The position of the Christiansen feature in aqueously and thermally altered CM chondrite spectra (excluding Wisconsin Range [WIS] 91600) against enstatite abundance as determined by position-sensitive-detector X-ray diffraction (PSD-XRD).

As features in the Si-O bending region (wavelengths  $>18 \mu\text{m}$ ) are more identifiable in emissivity spectra compared to reflectance spectra, trends with aqueous alteration at longer wavelengths can be evaluated. This is valuable as features in this region have been identified in OTES spectra of Bennu (Hamilton et al., 2019). Figure 8 compares the ambient and SAE emissivity spectra in this range for ALH 83100, ALH 83102, LON94101, and Murchison with the ambient emissivity spectrum of Mg-rich olivine and the reflectance spectrum of Mg-serpentine, both from Bates et al. (2020). The Murchison emissivity spectra show features consistent with Mg-rich olivine at 19.72, 21.07, 24.05, and 34.99  $\mu\text{m}$ , despite having  $\sim 75 \text{ vol\%}$  phyllosilicates and only  $\sim 15 \text{ vol\%}$  primary olivine (Howard et al., 2015), although XRD mineralogy and spectra were collected from different Murchison powders. Donaldson Hanna et al. (2019) showed that addition of as little as 5 vol% olivine to a predominately phyllosilicate physical mixture (85.5 vol%) changes the position of the CF, and the Murchison spectra here show that an olivine abundance of  $\sim 15 \text{ vol\%}$  is sufficient to superimpose olivine features over the broad phyllosilicate features in the Si-O bending region. In contrast, the more aqueously altered ALH 83100 and ALH 83102 spectra only show features in this region consistent with phyllosilicates (Figure 8) because they contain less primary olivine ( $\sim 8 \text{ vol\%}$ ) and more phyllosilicates ( $\sim 84 \text{ vol\%}$ ) (Table 1).

The LON 94101 ambient and SAE spectra show an intermediate behavior, consistent with it being less aqueously altered than ALH 83100 and ALH 83102. The spectra have a feature near 23.75  $\mu\text{m}$ , which is between the Mg-serpentine features identified in the ALH 83100 and ALH 83102 spectra

at 23.25  $\mu\text{m}$  and the olivine feature in the Murchison spectra at 24.05  $\mu\text{m}$ . The LON 94101 spectra have a phyllosilicate feature at 31.25  $\mu\text{m}$  and an olivine feature near 34.93  $\mu\text{m}$ , but do not show the Mg-olivine features near 19.72 and 21.07  $\mu\text{m}$  that are seen in the Murchison spectra. The result of this is a trend in this feature to shorter wavelengths with increasing aqueous alteration (Figure 8b). This supports conclusions from Hanna et al. (2020), who identified a feature within this 23.25–24.04  $\mu\text{m}$  Si-O bending region that shifted to shorter wavelengths as alteration increased.

#### 4.2.3. Thermal Alteration in MIR Emissivity Spectra

Features in the 5–8  $\mu\text{m}$  spectral range are observed in the emissivity spectra of most thermally altered samples. In aqueously altered chondrites, these have been associated with the presence of phyllosilicates (Bates et al., 2020), organics and adsorbed  $\text{H}_2\text{O}$  (Beck et al., 2018). Alemanno et al. (2020) showed vibrational features do remain in this range in the spectra of phyllosilicates that have been experimentally dehydrated, so the features observed in the stage II CM spectra may be due to disordered phyllosilicates. In the stage IV CM spectra, there are features near 6.10  $\mu\text{m}$ , consistent with bound molecular water. As suggested by the larger 3  $\mu\text{m}$  features in these sample spectra, PCA 02010 and PCA 02012 have terrestrial alteration products which may be contributing to these 6.10  $\mu\text{m}$  features. The samples were heated to 80°C and 75°C when collecting ambient and SAE emissivity spectra, however, so it is still likely that adsorbed water not contained within rust minerals was driven off. Olivine spectra also show features in this region (Baldridge et al., 2009; Bates et al., 2020; Christensen et al., 2000), and considering the olivine dominated mineralogy of PCA 02010 and PCA 02012, these phases may be responsible for the features at 6.10  $\mu\text{m}$ .

Most emissivity spectra show subtle features near 6.90  $\mu\text{m}$ . Carbonates are known to have features at these wavelengths (Beck et al., 2018; Lane & Christensen, 1997), and features at 6.90  $\mu\text{m}$  appear in emissivity spectra of mineral mixtures containing 5 vol% carbonates (Donaldson Hanna et al., 2019). However, the appearance of these features in the spectra here does not correlate with the abundance of carbonates (0–2 vol%, Table 1). The stage III CY Y 980115 spectra show an additional feature near 6.60  $\mu\text{m}$ , creating a doublet peak with the 6.90  $\mu\text{m}$  feature (Figure 5c). This is consistent with previous spectral observations of the CY chondrites. Miyamoto (1992) attributed the 6.60  $\mu\text{m}$  feature in a stage III CY (Y 82162, which was not included in this study) to terrestrial weathering products, and the 6.90  $\mu\text{m}$  feature to the incomplete break

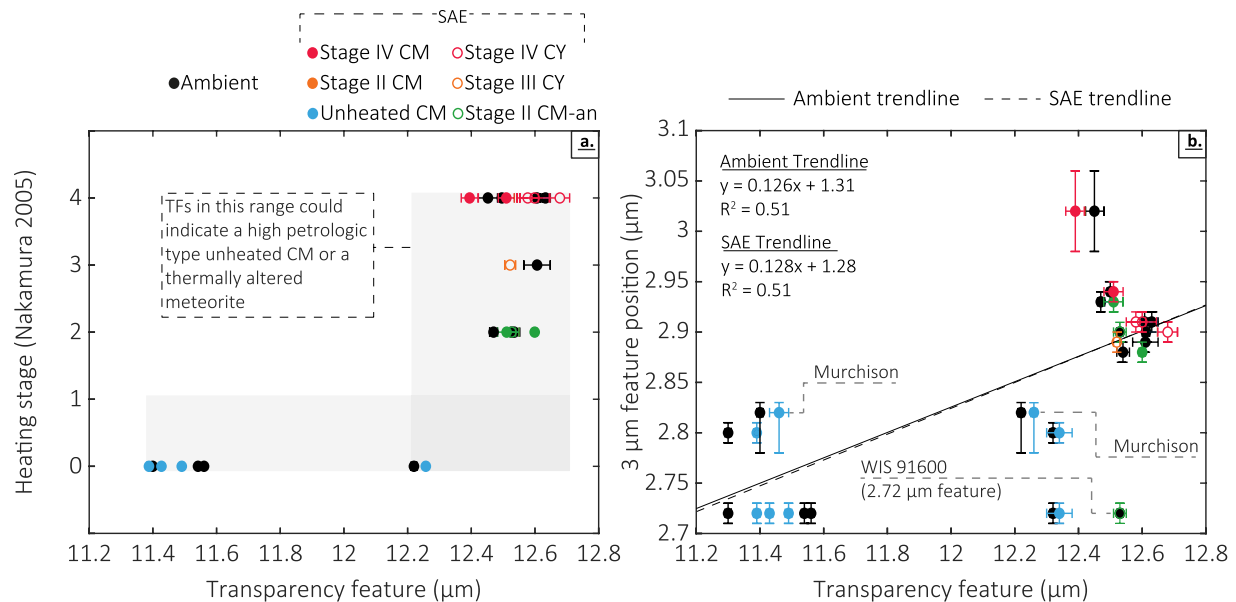


**Figure 10.** (a) The position of the transparency feature (TF) against heating stage. (b) The relationship between the position of the TF from the emissivity spectra and the position of the 3 μm feature from reflectance spectra of the same material. Note that error bars might be obscured by markers due to their small ranges. For meteorites which show multiple 3 μm features (Lonewolf Nunataks [LON] 94101 and Wisconsin Range [WIS] 91600), and multiple TFs (LON 94101 and Murchison), all possible combinations of features are plotted. The WIS 91600 2.72 μm feature was not included in the trend calculations. This relationship between different spectral parameters can help distinguish between the effects of aqueous and thermal alteration on the position of the TF.

down of calcite. It is not convincing that the 6.60 μm feature is a result of weathering, given that it is not present in spectra that show increased 3 μm band areas as a result of weathering products (e.g., PCA 02010), and the Y 980115 3 μm feature does not show an anomalously large area (Table 2, Figure 5a). A number of different carbonates have been identified in petrographic studies of the stage III CYs, including dolomite in Y 82029, Y 980115 and Y 82162 (Fujiya et al., 2013; King, Bates, et al., 2019), and also magnesite in Y 86029 (Tonui et al., 2003). These carbonates show features at shorter wavelengths than calcite, and it may be that the features in the stage III spectra reflect the different chemistries of the carbonates in the CYs compared to the CMs (Bandfield et al., 2003; Lane & Christensen, 1997). If there are carbonates present in the stage III samples however, they must have survived the metamorphism. Additionally, they are not identified in XRD patterns and so are in low abundance, therefore it is surprising they can be observed in the spectra. It is clear the causes of features in this region require further study. The 6.60 and 6.90 μm features are not observed in stage IV CY spectra (if they are due to carbonates this indicates these phases have fully broken down by the temperatures experienced by the stage IV samples), therefore their presence could be used to distinguish different degrees of thermal alteration in the CYs.

The CF is a complex region to disentangle in CM and CY chondrites due to the most abundant mineral phases in these meteorites (olivine and phyllosilicates) showing similar spectral ranges with overlapping CFs (Bates et al., 2020; Hamilton, 2010; Lane et al., 2011). An additional difficulty is how complex the shape of the features in the stage IV CY chondrite spectra are, resulting it in being challenging to accurately identify a single CF peak. Also of note is the difference between ambient and SAE emissivity measurements in the stage IV CY spectra, where not only the shape of the plateau changes, but the vibrational feature near 9.81 μm becomes indistinguishable. This suggests some minerals within the CY chondrites are not emitting in the same way as they did under ambient conditions and highlights the importance of measuring under appropriate conditions. Within the CM chondrites, the thermally altered sample spectra have CFs at shorter wavelengths (~8.80 μm in the stage II CM spectra and ~8.60 μm in the stage IV CM spectra, compared to ~9.10 μm in the ALH 83100, ALH 83102 and LON 94101 spectra). However, if the variation of CFs observed in aqueously altered CM chondrite spectra is considered, and Murchison, which has a CF at ~8.75 μm, is included in the analysis, this relationship is no longer true. The CF in the CM spectra seems not to reflect the degree of thermal alteration, but instead the presence of enstatite, shifting to shorter wavelengths with

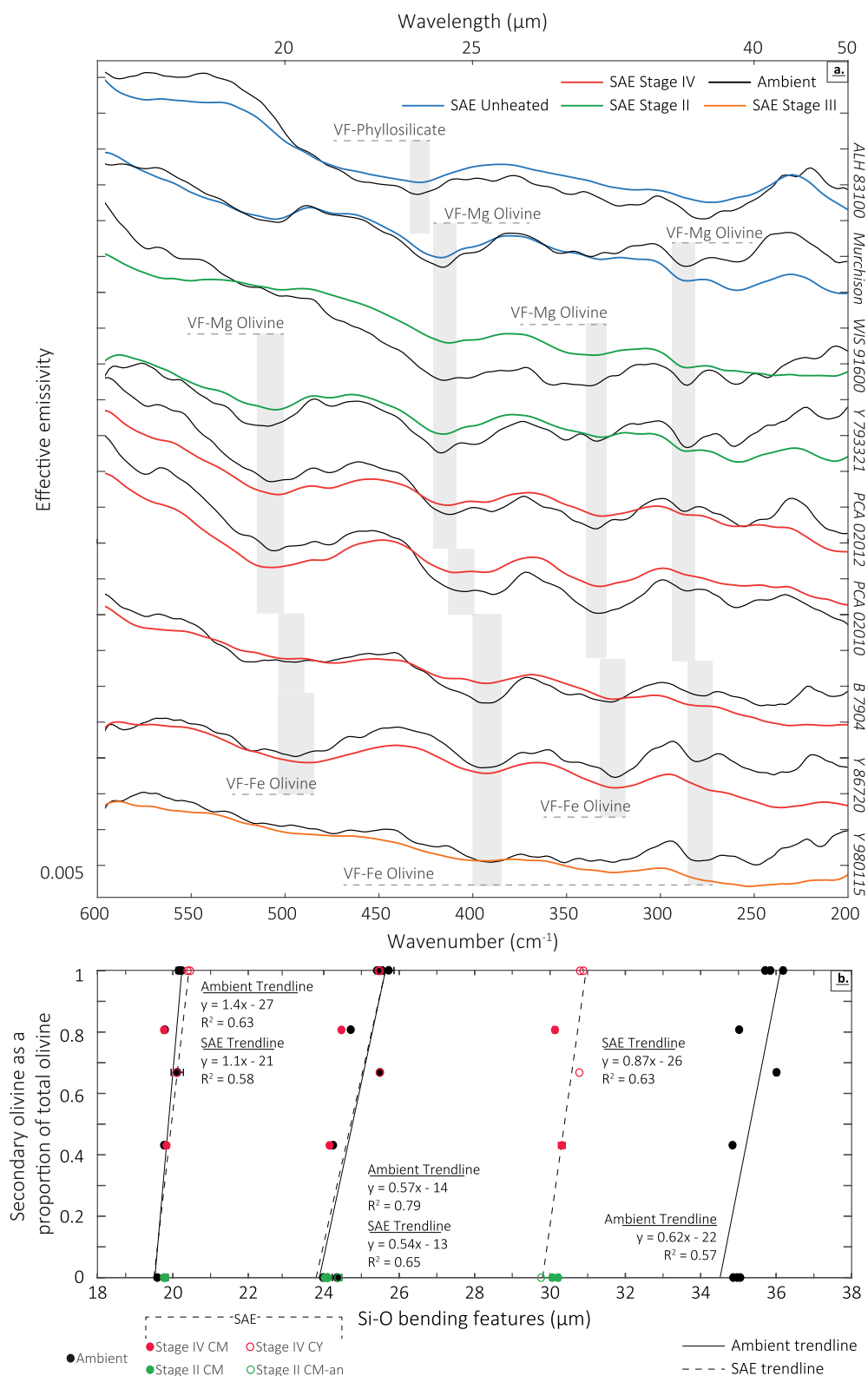
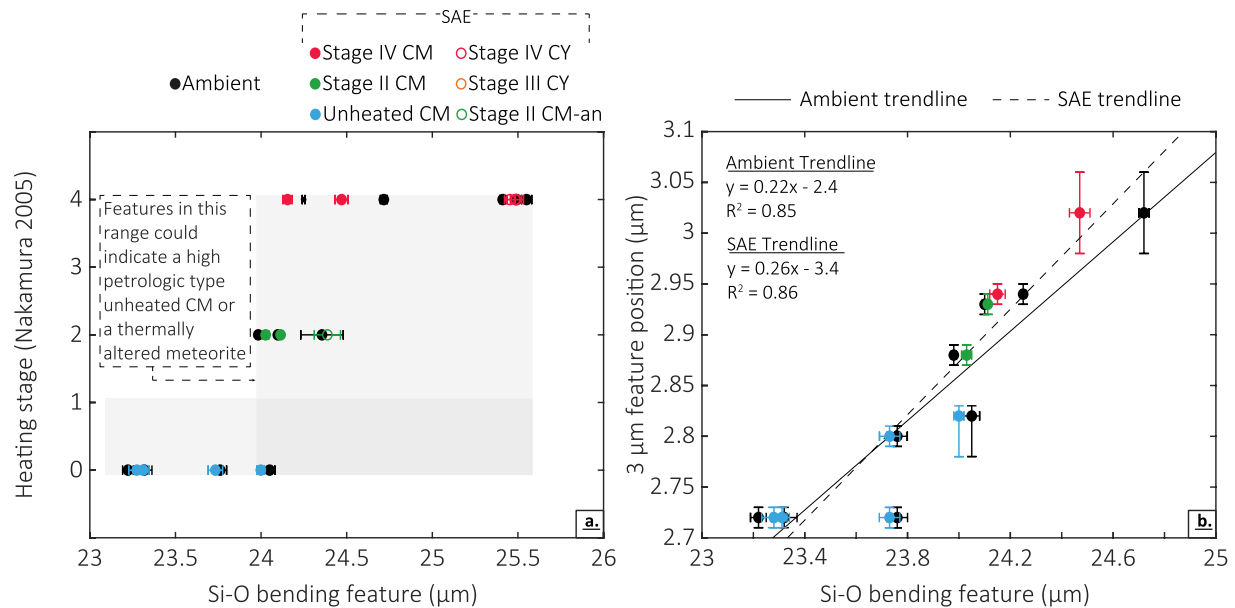


Figure 11



**Figure 12.** (a) The position of the Si-O bending feature between 23 and 26  $\mu\text{m}$  against heating stage. (b) The relationship between the position of the Si-O bending feature from the emissivity spectra of the aqueously and thermally altered CM chondrites and the position of the 3  $\mu\text{m}$  feature from reflectance spectra of the same material. Note that error bars might be obscured by markers due to their small ranges. For Lonewolf Nunataks (LON) 94101, which shows multiple 3  $\mu\text{m}$  features (2.72 and 2.80  $\mu\text{m}$ ), all possible combinations of features are plotted. This relationship between different spectral parameters can help distinguish between the effects of aqueous and thermal alteration on the position of the Si-O bending feature.

increasing abundance (Figure 9). Enstatite has a CF near 8.33  $\mu\text{m}$  (Donaldson Hanna, Wyatt, et al., 2012; Hamilton, 2000). The enstatite abundance cannot however be associated with different degrees of thermal alteration as there does not appear to be a consistent relationship between heating and enstatite abundance (Figure 9).

The position of the TF is at longer wavelengths in thermally altered sample spectra ( $>12.5 \mu\text{m}$ ), compared to the aqueously altered CM spectra (11.4–12.2  $\mu\text{m}$ ) (Figure 10a). This is likely because of higher olivine abundances in the stage III and stage IV CM and CY spectra: the emissivity spectrum of Mg-rich olivine has a transparency feature near 12.85  $\mu\text{m}$  (Bates et al., 2020; Donaldson Hanna, Wyatt, et al., 2012; Hamilton, 2010). Within the thermally altered (i.e., stage II to stage IV) spectra there is no convincing relationship between degree of thermal alteration and TF position. However, aqueously altered spectra with high petrologic types also have TFs at longer wavelengths: the Murchison spectra show doublet features with one of the minima near 12.24  $\mu\text{m}$ . Although this does not overlap with the TFs in the dehydrated samples, the trend does imply a less aqueously altered CM emissivity spectra would have a TF that does overlap. The effects of aqueous and thermal alteration can be distinguished by combining the TF position with the position of the 3  $\mu\text{m}$  feature, which is shown in Figure 10b, although this does not resolve between heating stages. The 3  $\mu\text{m}$  position was determined from the reflectance spectra of the same sample so combining observations from multiple spectral ranges can be done without the issue of different samples showing variable spectral features due to meteorite heterogeneity. Given the reflectance and emissivity spectra of Murchison were collected on different samples, the error of the 3  $\mu\text{m}$  feature in Figure 10b is increased to include values determined for multiple samples by previous studies (Calvin & King, 1997; Garenne et al., 2016; Hanna et al., 2020; Miyamoto, 1992; Takir et al., 2013). Figure 10b shows the position of the TF is correlated with the position of the 3  $\mu\text{m}$  feature and the two can be used to distinguish between aqueous

**Figure 11.** (next page) (a) The Si-O bending region, between 16.7 and 50  $\mu\text{m}$  from the emissivity spectra of representative CM, CM-an, and CY chondrites, including the emissivity spectra of Murchison. Ambient and simulated asteroid environment (SAE) spectra are offset so they plot on top of each other for the same meteorite. (b) The position of features in the Si-O bending region against secondary olivine as a proportion of total anhydrous silicate as determined through position-sensitive-detector X-ray diffraction (PSD-XRD). VF indicates vibrational features, and note that error bars might be obscured by markers due to their small ranges. Features show a shift to longer wavelengths with increasing secondary olivine.



and thermal alteration. This highlights the advantages of measuring over multiple wavelength ranges to provide more robust mineralogical determinations.

Figure 11 shows the spectra between  $\sim 16.5$  and  $50\ \mu\text{m}$  for representative aqueously altered CM and thermally altered CM, CM-an, and CY spectra. In the thermally altered CM and CY spectra, we observe features in this region consistent with olivine, although the positions of these features are at longer wavelengths for the CYs than the CMs. Features at longer wavelengths are consistent with the olivine containing more iron (Hamilton, 2010; Lane et al., 2011), in agreement with the mineralogy of the CY chondrites (Table 1). Y 86720, Y 86789, and Y 980115 experienced near complete aqueous alteration prior to thermal metamorphism, so contain abundant Fe-rich secondary olivine and no primary Mg-rich olivine. In contrast, the thermally altered CM chondrites typically contain primary olivine (11–27 vol%, Table 1), which influences the position of features, shifting them to shorter wavelengths. This results in features at longer wavelengths observed in the spectra of thermally altered samples with more secondary olivine (Figure 11b). Additionally, TEM studies and XRD analysis shows that the secondary olivine is poorly crystalline (Nakamura, 2005), and we observe this as a “smoothing out” of spectral features, particularly under SAE conditions. Poorly crystalline or amorphous phases have been shown to have broader features with less spectral structure than seen in the spectra of more crystalline materials (e.g., Hamilton et al., 2020; Minitti & Hamilton, 2010).

PCA 02010 and B 7904 both contain primary Mg-rich olivine ( $\sim 15$  and  $\sim 25$  vol%, respectively) and significant secondary olivine ( $\sim 61$  and  $\sim 50$  vol%, respectively). Figures 11b shows that the positions of features between 18 and  $38\ \mu\text{m}$  can help constrain the abundance of the secondary olivine in these samples, as they show features at longer wavelengths than observed in samples with no secondary olivine. The presence of primary olivine can be confirmed by looking at other wavelength ranges, for example in the Si-O stretching region the B 7904 and PCA 02010 ambient spectra show features at  $9.73$  and  $10.72\ \mu\text{m}$ , and  $9.85$  and  $10.66\ \mu\text{m}$ , respectively. Combining observations across multiple wavelength ranges can therefore help identify the presence of both primary and secondary olivine. It should be noted that in this case the more Fe-rich olivine can be confirmed as secondary based on XRD analyses and known mineralogy, however when comparing to remote observations this parameter would only be able to identify Fe-rich olivine, not the fact it is secondary.

Figure 12 shows more specifically how the feature between  $23$  and  $26\ \mu\text{m}$  is positioned in aqueously and thermally altered samples. Figure 12a shows we observed a shift in the feature to longer wavelengths with thermal alteration. However, as with the TF, this shift to longer wavelengths is also consistent with a lower degree of aqueous alteration: the Murchison spectra shows a feature similar to that observed in the stage II and stage IV spectra due to its higher olivine abundances compared to ALH 83100, ALH 83102, and LON 94101 (Table 1). In order to help distinguish between aqueous and thermal alteration, the Si-O bending feature can be combined with the position of the  $3\ \mu\text{m}$  feature (Figure 12b). This relationship only works for the aqueously altered and dehydrated CM chondrites, as the CY chondrite features are influenced by the presence of only secondary olivine, shifting the features to even longer wavelengths, but not changing the position of the  $3\ \mu\text{m}$  feature. As in Figure 10b, the error for the Murchison  $3\ \mu\text{m}$  feature is increased to include determinations from previous studies.

#### 4.3. Comparisons With Ryugu and Bennu Spectra

Spectra collected by NIRS3 of the surface and exposed subsurface of asteroid Ryugu show a flat, featureless spectral slope at wavelengths  $< 2.5\ \mu\text{m}$ , and a shallow, narrow absorption at  $2.72\ \mu\text{m}$  consistent with the presence of Mg-rich phyllosilicates (Kitazato et al., 2019, 2021). The albedo of the surface of Ryugu is also lower ( $4.5 \pm 0.2\%$ , Kitazato et al., 2019) than most laboratory measurements of carbonaceous chondrites, apart from some spectra of CY chondrites and experimentally dehydrated CI chondrites (King et al., 2017; Kitazato et al., 2019, 2021). Additionally, the shallow depth of the  $2.72\ \mu\text{m}$  feature best matches the spectra of experimentally dehydrated (to  $500^\circ\text{C}$ ) Ivuna and MET 01072, a shocked CM2 (Kitazato et al., 2019). It has therefore been suggested that the surface of Ryugu has experienced some degree of dehydration (Michel et al., 2020; Sugita et al., 2019). The  $3\ \mu\text{m}$  feature of Ryugu can be compared to the NIR spectra presented in this study in order to evaluate whether the asteroid has a similar composition to thermally altered CM or CY meteorites.

We find that the thermally altered CM and CY chondrites do not show a feature near 2.72  $\mu\text{m}$  and instead have broad features with centers between 2.88 and 3.04  $\mu\text{m}$  (Figures 2,3, and 5). The lack of this feature in even the moderately dehydrated stage II samples suggests these thermally altered CM and CY chondrites may not be a good representation of the globally averaged surface composition of Ryugu, or at least that the heating these meteorites experienced may not be an adequate representation of the metamorphism on Ryugu. The NIR spectrum of WIS 91600 does show a weak 2.72  $\mu\text{m}$  feature consistent with the partial dehydration of smectite-like phyllosilicates. As the surface of Ryugu is dehydrated but its spectrum still shows a 2.72  $\mu\text{m}$  feature, this could imply a similar composition of dehydrated Mg-rich smectite phyllosilicates as observed in WIS 91600. As suggested, the presence of smectites may indicate WIS 91600, and therefore Ryugu, share some affinity with CI chondrites. Both the CI parent body(ies) and the WIS 9600 parent body are hypothesized to have formed in the outer Solar System, >10 AU (Bryson et al., 2020; Desch et al., 2018). If Ryugu shares some affinities with these meteorites, it might imply its parent body formed in the outer Solar System before migrating inwards during periods of early giant planet migration (e.g., Walsh et al., 2011).

OVIRS observations of asteroid Bennu show a 3  $\mu\text{m}$  feature with a larger band depth than that observed in the Ryugu spectrum, with a band center near  $2.74 \pm 0.01 \mu\text{m}$  (Hamilton et al., 2019), suggesting that Bennu has experienced a high degree of aqueous alteration. This is within error of the 3  $\mu\text{m}$  features in the ALH 83100 and ALH 83102 spectra, although the Bennu feature is not as sharp or well-defined as those for the meteorites. ALH 83100 and ALH 83102 are highly aqueously altered, with PSF petrologic types of 1.2–1.3, so this observation supports the hypothesis that Bennu is highly aqueously altered. The OTES spectra collected from the Preliminary Survey phase of the OSIRIS-REx mission also show some similarity with these CM chondrite spectra, with a CF near 9.00  $\mu\text{m}$  and a Si-O bending feature near 22.70  $\mu\text{m}$  (Hamilton et al., 2019). The MIR spectral range is sensitive to particle size (e.g., Salisbury, 1993; Shirley & Glotch, 2019), and some spectral parameters will only be applicable to fine particulate material. For example, the TF is only distinguishable in optically thin material, or a fine particulate size (<75  $\mu\text{m}$ , Salisbury, 1993). The meteorite spectra from this study will therefore only be comparable to regions of the surface of Bennu (and Ryugu) spectrally dominated by fines. Nevertheless, the spectra in this study support the hypothesis that there are widespread Mg-serpentines on the surface of Bennu. For example, the Si-O bending feature at 22.70  $\mu\text{m}$  would correspond to a PSF petrologic type of 1.0 based on the trend shown in Figures 11b, implying near complete aqueous alteration of the surface. Additionally, the Si-O bending feature and 3  $\mu\text{m}$  feature, when plotted along the trend shown in Figure 12b indicate the surface has likely not experienced any thermal alteration. However, more recent observations by OVIRS during the mapping phases of OSIRIS-REx have confirmed the presence of anhydrous, pyroxene-rich boulders on Bennu hypothesized to be exogeneous (DellaGiustina et al., 2020), indicating the surface composition is not homogeneous. The position of the CF in the Bennu Preliminary Survey spectrum at 9.00  $\mu\text{m}$  does correspond to an enstatite abundance of ~4 vol% (based on the trend in Figure 9), however this spectrum was a global average and not high spatial resolution spectra of the specific areas the boulders were identified. OTES did observe the specific areas the pyroxene rich boulders were identified, however no spectral absorptions associated with pyroxene were identified (DellaGiustina et al., 2020). However, as shown by the influence of pyroxene on the spectra in this study, future analyses of the OTES spectra of regions with the pyroxene-rich boulders might provide more fruitful comparisons. It is likely that further analysis of the Bennu spectra will show additional variable composition. The spectra in this study should help to identify not only aqueously altered material but also should help to distinguish between anhydrous and dehydrated material on the Bennu surface.

## 5. Conclusions

We have collected MIR emissivity spectra between 5.5 and 50  $\mu\text{m}$  from 12 aqueously and thermally altered CM and CY chondrite powders for which the bulk mineralogy was determined using PSD-XRD. The MIR emissivity spectra were collected under both ambient and SAE conditions that replicated the surface of Bennu, target of the OSIRIS-REx mission. In addition, we also acquired reflectance spectra of the powders between 2 and 5  $\mu\text{m}$ .

We find trends in the emissivity MIR spectra of CM chondrites related to their degree of aqueous alteration that are consistent with trends previously reported in MIR reflectance spectra:

1. The CF becomes sharper as aqueous alteration increases (observed by McAdam et al., 2015 and Bates et al., 2020) and shifts to longer wavelengths (observed by Hanna et al., 2020).
2. The TF shifts to shorter wavelengths with increasing aqueous alteration (observed by McAdam et al., 2015 and Bates et al., 2020).
3. The Si-O bending feature between 23 and 26  $\mu\text{m}$  shifts to shorter wavelengths with increasing aqueous alteration (observed by Hanna et al., 2020).

Although these trends were retained between reflectance and emissivity spectra, we emphasize the need for measurements under appropriate environmental conditions. For example, Bates et al. (2020) found the CF to shift to shorter wavelengths with increasing aqueous alteration in powder reflectance spectra, however, an opposite trend was observed here, in better agreement with the MIR characterization of polished sections by Hanna et al., (2020). We also discuss the difference between measuring emissivity under ambient and SAE conditions, noting that there are differences in spectral shape and feature position due to the introduction of a thermal gradient. This must be considered when observing airless bodies.

In addition to identifying trends associated with hydration, we identified parameters in NIR reflectance and MIR emissivity spectra related to the dehydrated mineralogy and alteration history of thermally metamorphosed CM and CY chondrites:

- The 3  $\mu\text{m}$  feature becomes rounder, shifts to longer wavelengths, and is reduced in area and depth in dehydrated meteorite spectra.
- Meteorites that contain dehydrated smectite material may retain a sharp 3  $\mu\text{m}$  feature.
- The TF and Si-O bending features both shift to longer wavelengths with increasing metamorphic temperature in CM chondrite spectra, although this may also be the result of a lower degree of aqueous alteration. In order to distinguish alteration schemes, these features need to be combined with the 3  $\mu\text{m}$  feature position.
- Features in the Si-O bending region are also sensitive to olivine chemistry, shifting to longer wavelengths with increasing abundance of Fe-rich secondary olivine.

We identified parameters which can be used to distinguish between aqueously altered CM spectra and dehydrated CM and CY spectra, especially when combining parameters from both NIR and MIR wavelength ranges (i.e., 3  $\mu\text{m}$  compared to the positions of TF and Si-O bending features). Trends within the dehydrated meteorite spectra were distinct in wavelength ranges where vibrational features due to variable olivine chemistries were easily distinguishable.

The parameters determined in this study can be used to interpret spectral observations of Ryugu and Bennu. For example, the 2.72  $\mu\text{m}$  feature in the Ryugu spectrum shows some similarity to the feature observed in the WIS 91600 spectrum, suggesting the possible presence of smectite phyllosilicates on the asteroid surface. Additionally, the OTES spectrum of Bennu is similar to the spectra collected from hydrated CM chondrites, supporting the conclusions the Bennu surface is aqueously altered. The spectra presented here may also provide additional parameters for determining the presence of pyroxene rich material on the Bennu surface, due to the result that the CF is sensitive to pyroxene abundance. The spectra presented here will help to interpret results from higher spatial resolution spectral observations of Ryugu and Bennu collected during mapping phases and should aid identification of phyllosilicate and olivine compositions. Additionally, comparing these spectra to spectra of other meteorite types will enable areas of dehydration on the asteroid surfaces to be distinguished from anhydrous material that was never aqueously altered.

## Data Availability Statement

Datasets for this research are available at the Oxford University Research Archive in Bates et al. (2021a) and Bates et al. (2021b).

## Acknowledgments

The authors would like to thank Antarctic Search for Meteorites (ANSMET), U.S.A. and the National Institute for Polar Research (NIPR), Japan for providing meteorite samples investigated in this study. They also thank Jens Najorka and Paul Schofield for assistance with XRD analysis and data interpretation. Thanks also go to Christopher Haberle and Michael Bramble for their constructive comments which greatly improved this manuscript. This work was supported by the Science and Technology Facilities Council (STFC), UK, through grant 1860431.

## References

- Alemanno, G., Maturilli, A., Helbert, J., & D'Amore, M. (2020). Laboratory studies on the 3  $\mu\text{m}$  spectral features of Mg-rich phyllosilicates with temperature variations in support of the interpretation of small asteroid surface spectra. *Earth and Planetary Science Letters*, 546, 116424. <https://doi.org/10.1016/j.epsl.2020.116424>
- Alexander, C. M. O'D. (2017). The origin of inner solar system water. *Philosophical Transactions of the Royal Society*, 375, 20150384. <https://doi.org/10.1098/rsta.2015.0384>
- Alexander, C. M. O'D., Bowden, R., Fogel, M. L., Howard, K. T., Herd, C. D. K., & Nittler, L. R. (2012). The provenances of asteroids, and their contributions to the volatile inventories of the terrestrial planets. *Science*, 337, 721–723. <https://doi.org/10.1126/science.1223474>
- Alexander, C. M. O. D., Greenwood, R. C., Bowden, R., Gibson, J. M., Howard, K. T., & Franchi, I. A. (2018). A multi-technique search for the most primitive CO chondrites. *Geochimica et Cosmochimica Acta*, 221, 406–420. <https://doi.org/10.1016/j.gca.2017.04.021>
- Alexander, C. M. O'D., Howard, K. T., Bowden, R., & Fogel, M. L. (2013). The classification of CM and CR chondrites using bulk H, C and N abundances and isotopic compositions. *Geochimica et Cosmochimica Acta*, 123, 244–260. <https://doi.org/10.1016/j.gca.2013.05.019>
- Baldrige, A. M., Hook, S. J., Grove, C. I., & Rivera, G. (2009). The ASTER spectral library version 2.0. *Remote Sensing of Environment*, 113, 711–715. <https://doi.org/10.1016/j.rse.2008.11.007>
- Bandfield, J. L., Glotch, T. D., & Christensen, P. R. (2003). Spectroscopic identification of carbonate minerals in the Martian dust. *Science*, 301, 1084–1087. <https://doi.org/10.1126/science.1088054>
- Barnes, J. J., Kring, D. A., Tartese, R., Franchi, I. A., Anand, M., & Russell, S. S. (2016). An asteroidal origin for water in the Moon. *Nature Communications*, 7, 1–10. <https://doi.org/10.1038/ncomms11684>
- Bates, H. C., Donaldson Hanna, K. L., King, A. J., Bowles, N. E., & Russell, S. S. (2021a). *Spectral data of aqueously and thermally altered carbonaceous chondrites*. University of Oxford 10.5287/bodleian:2NxMjAzwedataset.
- Bates, H. C., Donaldson Hanna, K. L., King, A. J., Bowles, N. E., & Russell, S. S. (2021b). *X-ray diffraction data of aqueously and thermally altered carbonaceous chondrites*. University of Oxford 10.5287/bodleian:ozM5ZQP1Ndaset.
- Bates, H. C., King, A. J., Donaldson Hanna, K. L., Bowles, N. E., & Russell, S. S. (2020). Linking mineralogy and spectroscopy of highly aqueously altered CM and CI carbonaceous chondrites in preparation for primitive asteroid sample return. *Meteoritics & Planetary Sciences*, 55, 77–101. <https://doi.org/10.1111/maps.13411>
- Beck, P., Maturilli, A., Garenne, A., Vernazza, P., Helbert, J., Quirico, E., & Schmitt, B. (2018). What is controlling the reflectance spectra (0.35–150  $\mu\text{m}$ ) of hydrated (and dehydrated) carbonaceous chondrites? *Icarus*, 313, 124–138. <https://doi.org/10.1016/j.icarus.2018.05.010>
- Beck, P., Quirico, E., Montes-Hernandez, G., Bonal, L., Bollard, J., Orthous-Daunay, F.-R., et al. (2010). Hydrous mineralogy of CM and CI chondrites from infrared spectroscopy and their relationship with low albedo asteroids. *Geochimica et Cosmochimica Acta*, 74, 4881–4892. <https://doi.org/10.1016/j.gca.2010.05.020>
- Bishop, J. L., Lane, M. D., Dyar, M. D., & Brown, A. J. (2008). Reflectance and emission spectroscopy study of four groups of phyllosilicates: Smectites, kaolinite-serpentines, chlorites and micas. *Clay Minerals*, 43, 35–54. <https://doi.org/10.1180/claymin.2008.043.1.03>
- Bland, P. A., Cressey, G., & Menzies, O. N. (2004). Modal mineralogy of carbonaceous chondrites by X-ray diffraction and Mössbauer spectroscopy. *Meteoritics & Planetary Sciences*, 39, 3–16. <https://doi.org/10.1111/j.1945-5100.2004.tb00046.x>
- Brearely, A. J. (2006). The action of water. In D. S. Lauretta, & H. Y. McSween (Eds.), *Meteorites and the early solar system II* (pp. 587–624). The University of Arizona Press.
- Bryson, J. F. J., Weiss, B. P., Biersteker, J. B., King, A. J., & Russell, S. S. (2020). Constraints on the distances and timescales of solid migration in the early solar system from meteorite magnetism. *The Astrophysical Journal*, 896, 103. <https://doi.org/10.3847/1538-4357/ab91ab>
- Burbine, T. H., McCoy, T. J., Meibom, A., Gladman, B., & Keil, K. (2002). Meteoritic parent bodies: Their number and identification. *Asteroids III* (pp. 653–667).
- Calvin, W. M., & King, T. V. V. (1997). Spectral characteristics of iron bearing phyllosilicates: Comparison to Orgueil (CI1), Murchison and Murray (CM2). *Meteoritics & Planetary Sciences*, 32, 693–701. <https://doi.org/10.1111/j.1945-5100.1997.tb01554.x>
- Che, C., Glotch, T. D., Bish, D. L., Michalski, J. R., & Xu, W. (2011). Spectroscopic study of the dehydration and/or dehydroxylation of phyllosilicate and zeolite minerals. *Journal of Geophysical Research*, 116, E05007. <https://doi.org/10.1029/2010JE003740>
- Christensen, P. R., Bandfield, J. L., Hamilton, V. E., Howard, D. A., Lane, M. D., Piatek, J. L., et al. (2000). A thermal emission spectral library of rock-forming minerals. *Journal of Geophysical Research*, 105, 9735–9739. <https://doi.org/10.1029/1998JE000624>
- Christensen, P. R., Hamilton, V. E., Mehall, G. L., Pelham, D., O'Donnell, W., Anwar, S., et al. (2018). The OSIRIS-REx Thermal Emission Spectrometer (OTES) instrument. *Space Science Reviews*, 214, 87. <https://doi.org/10.1007/s11214-018-0513-6>
- Clark, B. E., Ziffer, J., Nesvorniy, D., Campins, H., Rivkin, A. S., Hiroi, T., et al. (2010). Spectroscopy of B-type asteroids: Subgroups and meteorite analogs. *Journal of Geophysical Research*, 115, 1–22. <https://doi.org/10.1029/2009JE003478>
- Cloutis, E. A., Hiroi, T., Gaffey, M. J., Alexander, C. M. O'D., & Mann, P. (2011). Spectral reflectance properties of carbonaceous chondrites: 1. CI chondrites. *Icarus*, 212, 180–209. <https://doi.org/10.1016/j.icarus.2010.12.009>
- Cressey, G., & Schofield, P. F. (1996). Rapid whole-pattern profile-stripping method for the quantification of multiphase samples. *Powder Diffraction*, 11, 35–39. <https://doi.org/10.1017/s0885715600008885>
- DellaGiustina, D. N., Kaplann, H. H., Simon, A. A., Bottke, W. F., Avdellidou, C., Delbo, M., et al. (2020). Exogenic basalt on asteroid (101955) Bennu. *Nature Astronomy*, 1–8, 31–38. <https://doi.org/10.1038/s41550-020-1195-z>
- Desch, S. J., Kalyaan, A., O', C. M., & Alexander, D. (2018). The eEffect of Jupiter's formation on the distribution of refractory elements and inclusions in meteorites. *The Astrophysical Journal Supplement Series*, 238, 11–42. <https://doi.org/10.3847/1538-4365/aad95f>
- Donaldson Hanna, K. L., Bowles, N. E., Warren, T., Hamilton, V. E., Schrader, D. L., McCoy, T. J., et al. (2021). Spectral characterization of Bennu analogs using PASCAL: A new experimental set-up for simulating the near-surface conditions of airless bodies. *Journal of Geophysical Research: Planets*, 126. <https://doi.org/10.1029/2020JE006624>
- Donaldson Hanna, K. L., Schrader, D. L., Cloutis, E. A., Cody, G. D., King, A. J., McCoy, T. J., et al. (2019). Spectral characterization of analog samples in anticipation of OSIRIS-REx's arrival at Bennu: A blind test study. *Icarus*, 319, 701–723. <https://doi.org/10.1016/j.icarus.2018.10.018>
- Donaldson Hanna, K. L., Thomas, I. R., Bowles, N. E., Greenhagen, B. T., Pieters, C. M., Mustard, J. F., et al. (2012). Laboratory emissivity measurements of the plagioclase solid solution series under varying environmental conditions. *Journal of Geophysical Research*, 117. <https://doi.org/10.1029/2012JE004184>
- Donaldson Hanna, K. L., Wyatt, M. B., Thomas, I. R., Bowles, N. E., Greenhagen, B. T., Maturilli, A., et al. (2012). Thermal infrared emissivity measurements under a simulated lunar environment: Application to the diviner lunar radiometer experiment. *Journal of Geophysical Research*, 117. <https://doi.org/10.1029/2011JE003862>



- Endress, M., Zinner, E. K., & Bischoff, A. (1996). Early aqueous activity on primitive meteorite parent bodies. *Nature*, 379, 701–703. <https://doi.org/10.1038/379701a0>
- Farmer, V. C. (1974). *The infrared spectra of minerals*. Mineralogical Society of Great Britain and Ireland. <https://doi.org/10.1180/mono-4>
- Fornasier, S., Lantz, C., Perna, D., Campins, H., Barucci, M. A., & Nesvorný, D. (2016). Spectral variability on primitive asteroids of the Themis and Beagle families: Space weathering effects or parent body heterogeneity? *Icarus*, 269, 1–14. <https://doi.org/10.1016/j.icarus.2016.01.002>
- Fujiya, W., Sugiura, N., Sano, Y., & Hiyagon, H. (2013). Mn-Cr ages of dolomites in CI chondrites and the Tagish Lake ungrouped carbonaceous chondrite. *Earth and Planetary Science Letters*, 362, 130–142. <https://doi.org/10.1016/j.epsl.2012.11.057>
- Gaffey, S. J., McFadden, L. A., Nash, D., & Pieters, C. M. (1993). Ultraviolet, visible, and near-infrared reflectance spectroscopy: Laboratory spectra of geologic materials. In C. M. Pieters, & P. A. Englert (Eds.), *Remote geochemical analysis: Elemental and mineralogical composition* (pp. 43–79). Cambridge University Press.
- Garenne, A., Beck, P., Montes-Hernandez, G., Brissaud, O., Schmitt, B., Quirico, E., et al. (2016). Bidirectional reflectance spectroscopy of carbonaceous chondrites: Implications for water quantification and primary composition. *Icarus*, 264, 172–183. <https://doi.org/10.1016/j.icarus.2015.09.005>
- Garenne, A., Beck, P., Montes-Hernandez, G., Chiriac, R., Toche, F., Quirico, E., et al. (2014). The abundance and stability of “water” in type 1 and 2 carbonaceous chondrites (CI, CM and CR). *Geochimica et Cosmochimica Acta*, 137, 93–112. <https://doi.org/10.1016/j.gca.2014.03.034>
- Grossman, J. N. (1994). The Meteoritical Bulletin, No. 76, 1994 January: The U.S. Antarctic meteorite collection. *Meteoritics*, 29. <https://doi.org/10.1111/j.1945-5100.1994.tb00661.x>
- Grott, M., Knollenberg, J., Borgs, B., Hänschke, F., Kessler, E., Helbert, J., et al. (2017). The MASCOT radiometer MARA for the Hayabusa 2 mission. *Space Science Reviews*, 208, 413–431. <https://doi.org/10.1007/s11214-016-0272-1>
- Hamilton, V. E. (2000). Thermal infrared emission spectroscopy of the pyroxene mineral series. *Journal of Geophysical Research*, 105, 9701–9716. <https://doi.org/10.1029/1999JE001112>
- Hamilton, V. E. (2010). Thermal infrared (vibrational) spectroscopy of Mg-Fe olivines: A review and applications to determining the composition of planetary surfaces. *Geochemistry*, 70, 7–33. <https://doi.org/10.1016/j.chemer.2009.12.005>
- Hamilton, V. E., Haberle, C. W., & Mayerhöfer, T. G. (2020). Effects of small crystallite size on the thermal infrared (vibrational) spectra of minerals. *American Mineralogist*, 105, 1756–1760. <https://doi.org/10.2138/am-2020-7602>
- Hamilton, V. E., Simon, A. A., Christensen, P. R., Reuter, D. C., Blark, B. E., Barucci, M. A., et al. (2019). Evidence for widespread hydrated minerals on asteroid (101955) Benu. *Nature Astronomy*, 3, 332–340. <https://doi.org/10.1038/s41550-019-0722-2>
- Hanna, R. D., Hamilton, V. E., Haberle, C. W., King, A. J., Abreu, N. M., & Friedrich, J. M. (2020). Distinguishing relative aqueous alteration and heating among CM chondrites with IR spectroscopy. *Icarus*, 346, 113760. <https://doi.org/10.1016/j.icarus.2020.113760>
- Henderson, B. G., & Jakosky, B. M. (1994). Near-surface thermal gradients and their effects on mid-infrared emission spectra of planetary surfaces. *Journal of Geophysical Research*, 99, 19063–19073. <https://doi.org/10.1029/94je01861>
- Hergenrother, C. W., Antonietta Barucci, M., Barnouin, O., Bierhaus, B., Binzel, R. P., Bottke, W. F., et al. (2014). *The design reference asteroid for the OSIRIS-REx mission target*. Benu.
- Hiroi, T., & Pieters, C. M. (1996). Reflectance spectra (UV–3  $\mu\text{m}$ ) of heated Ivuna (CI) meteorite and newly identified thermally metamorphosed CM chondrites. *27th lunar and planetary science conference* (pp. 551–552).
- Hiroi, T., Pieters, C. M., Zolensky, M. E., & Lipschutz, M. E. (1993). Evidence of thermal metamorphism on the C,G,B, and F asteroids. *Science*, 261, 1016–1018. <https://doi.org/10.1126/science.261.5124.1016>
- Hiroi, T., Zolensky, M. E., & Pieters, C. M. (1997). Characterization of unusual CI/CM/CR meteorites from reflectance spectroscopy. *28th lunar and planetary science conference* (pp. 577–578).
- Hiroi, T., Zolensky, M. E., Pieters, C. M., & Lipschutz, M. E. (1996). Thermal metamorphism of the C, G, B, and F asteroids seen from the 0.7  $\mu\text{m}$ , 3  $\mu\text{m}$ , and UV absorption strengths in comparison with carbonaceous chondrites. *Meteoritics & Planetary Sciences*, 31, 321–327. <https://doi.org/10.1111/j.1945-5100.1996.tb02068.x>
- Howard, K. T., Alexander, C. M. O., Schrader, D. L., & Dyl, K. A. (2015). Classification of hydrous meteorites (CR, CM and C2 ungrouped) by phyllosilicate fraction: PSD-XRD modal mineralogy and planetesimal environments. *Geochimica et Cosmochimica Acta*, 149, 206–222. <https://doi.org/10.1016/j.gca.2014.10.025>
- Howard, K. T., Benedix, G. K., Bland, P. A., & Cressey, G. (2009). Modal mineralogy of CM2 chondrites by X-ray diffraction (PSD-XRD). Part 1: Total phyllosilicate abundance and the degree of aqueous alteration. *Geochimica et Cosmochimica Acta*, 73, 4576–4589. <https://doi.org/10.1016/j.gca.2009.04.038>
- Howard, K. T., Benedix, G. K., Bland, P. A., & Cressey, G. (2011). Modal mineralogy of CM chondrites by X-ray diffraction (PSD-XRD): Part 2. Degree, nature and settings of aqueous alteration. *Geochimica et Cosmochimica Acta*, 75, 2735–2751. <https://doi.org/10.1016/j.gca.2011.02.021>
- Ikeda, Y. (1992). An overview of the research consortium, “Antarctic carbonaceous chondrites with CI affinities, Yamato-86720, Yamato-82162, and Belgica-7904”. *Proceedings of the NIPR Symposium on Antarctic Meteorites*, 5, 49–73.
- Iwata, T., Kitazato, K., Abe, M., Ohtake, M., Arai, T., Arai, T., et al. (2017). NIRS3: The near infrared spectrometer on Hayabusa2. *Space Science Reviews*, 208, 317–337. <https://doi.org/10.1007/s11214-017-0341-0>
- Kaplan, H. H., Lauretta, D. S., Simon, A. A., Hamilton, V. E., DellaGiustina, D. N., Golish, D. R., et al. (2020). Bright carbonate veins on asteroid (101955) Benu: Implications for aqueous alteration history. *Science*, 370. <https://doi.org/10.1126/science.abc3557>
- King, A. J., Bates, H. C., Krietsch, D., Busemann, H., Clay, P. L., Schofield, P. F., & Russell, S. S. (2019a). The Yamato-type (CY) carbonaceous chondrite group: Analogues for the surface of asteroid Ryugu? *Geochemistry*, 79, 125531. <https://doi.org/10.1016/j.chemer.2019.08.003>
- King, A. J., Russell, S. S., Schofield, P. F., Humphreys-Williams, E. R., Strekopytov, S., Abernethy, F. A. J., et al. (2019b). The alteration history of the Jbilet Winselwan CM carbonaceous chondrite: An analog for C-type asteroid sample return. *Meteoritics & Planetary Sciences*, 54, 521–543. <https://doi.org/10.1111/maps.13224>
- King, A. J., Schofield, P. F., Howard, K. T., & Russell, S. S. (2015). Modal mineralogy of CI and CI-like chondrites by X-ray diffraction. *Geochimica et Cosmochimica Acta*, 165, 148–160. <https://doi.org/10.1016/j.gca.2015.05.038>
- King, A. J., Schofield, P. F., & Russell, S. S. (2017). Type 1 aqueous alteration in CM carbonaceous chondrites: Implications for the evolution of water-rich asteroids. *Meteoritics & Planetary Sciences*, 52, 1197–1215. <https://doi.org/10.1111/maps.12872>
- King, A. J., Schofield, P. F., & Russell, S. S. (2021). Thermal alteration of CM carbonaceous chondrites: Mineralogical changes and metamorphic temperatures. *Geochimica et Cosmochimica Acta*, 298, 167–190. <https://doi.org/10.1016/j.gca.2021.02.011>
- Kitazato, K., Milliken, R. E., Iwata, T., Abe, M., Ohtake, M., Matsuura, S., et al. (2019). The surface composition of asteroid 162173 Ryugu from Hayabusa2 near-infrared spectroscopy. *Science*, 364, 272–275. <https://doi.org/10.1126/science.aav7432>



- Kitazato, K., Milliken, R. E., Iwata, T., Abe, M., Ohtake, M., Matsuura, S., et al. (2021). Thermally altered subsurface material of asteroid (162173) Ryugu. *Nature Astronomy*, 5, 246–250. <https://doi.org/10.1038/s41550-020-01271-2>
- Lane, M. D., & Christensen, P. R. (1997). Thermal infrared emission spectroscopy of anhydrous carbonates. *Journal of Geophysical Research*, 102, 25581–25592. <https://doi.org/10.1029/97JE02046>
- Lane, M. D., Glotch, T. D., Darby Dyar, M., Pieters, C. M., Klima, R., Hiroi, T., et al. (2011). Midinfrared spectroscopy of synthetic olivines: Thermal emission, specular and diffuse reflectance, and attenuated total reflectance studies of forsterite to fayalite. *Journal of Geophysical Research*, 116, 8010. <https://doi.org/10.1029/2010JE003588>
- Lauretta, D. S., Balram-Knutson, S. S., Beshore, E., Boynton, W. V., DAubigny, C. D., DellaGiustina, D. N., et al. (2017). OSIRIS-REx: Sample return from asteroid (101955) Bennu. *Space Science Reviews*, 212, 925–984.
- Lebofsky, L. A. (1980). Infrared reflectance spectra of asteroids: A search for water of hydration. *The Astronomical Journal*, 85. <https://doi.org/10.1086/112714>
- Lee, M. R., Lindgren, P., King, A. J., Greenwood, R. C., Franchi, I. A., & Sparkes, R. (2016). Elephant Moraine 96029, a very mildly aqueously altered and heated CM carbonaceous chondrite: Implications for the drivers of parent body processing. *Geochimica et Cosmochimica Acta*, 187, 237–259. <https://doi.org/10.1016/j.gca.2016.05.008>
- Lindgren, P., Lee, M. R., Sofo, M., & Burchell, M. J. (2011). Microstructure of calcite in the CM2 carbonaceous chondrite LON 94101: Implications for deformation history during and/or after aqueous alteration. *Earth and Planetary Science Letters*, 306, 289–298. <https://doi.org/10.1016/j.epsl.2011.04.022>
- Lipschutz, M. E., Zolensky, M. E., & Bell, M. S. (1999). New petrographic and trace element data on thermally metamorphosed carbonaceous chondrites. *Antarctic Meteorite Research*, 12, 57–80.
- Logan, L. M., Hunt, G. R., Salisbury, J. W., & Balsamo, S. R. (1973). Compositional implication of Christiansen frequency maximums for infrared remote sensing applications. *Journal of Geophysical Research*, 78, 430–450. <https://doi.org/10.1029/JB078i023p04983>
- Mahan, B., Moynier, F., Beck, P., Pringle, E. A., & Siebert, J. (2018). A history of violence: Insights into post-accretionary heating in carbonaceous chondrites from volatile element abundances, Zn isotopes and water contents. *Geochimica et Cosmochimica Acta*, 220, 19–35. <https://doi.org/10.1016/j.gca.2017.09.027>
- Marty, B. (2012). The origins and concentrations of water, carbon, nitrogen and noble gases on Earth. *Earth and Planetary Science Letters*, 313, 56–66. <https://doi.org/10.1016/j.epsl.2011.10.040>
- Matsuoka, K., Nakamura, T., Nakamura, Y., & Takaoka, N. (1996). Yamato-86789: A heated CM-like carbonaceous chondrite. *Proceedings of the NIPR Symposium on Antarctic Meteorites*, 9, 20–26.
- McAdam, M. M., Sunshine, J. M., Howard, K. T., & McCoy, T. M. (2015). Aqueous alteration on asteroids: Linking the mineralogy and spectroscopy of CM and CI chondrites. *Icarus*, 245, 320–332. <https://doi.org/10.1016/j.icarus.2014.09.041>
- Michalski, J. R., Kraft, M. D., Sharp, T. G., Williams, L. B., & Christensen, P. R. (2006). Emission spectroscopy of clay minerals and evidence for poorly crystalline aluminosilicates on Mars from Thermal Emission Spectrometer data. *Journal of Geophysical Research*, 111, E03004. <https://doi.org/10.1029/2005JE002438>
- Michel, P., Ballouz, R. L., Barnouin, O. S., Jutzi, M., Walsh, K. J., May, B. H., et al. (2020). Collisional formation of top-shaped asteroids and implications for the origins of Ryugu and Bennu. *Nature Communications*, 11, 1–11. <https://doi.org/10.1038/s41467-020-16433-z>
- Minitti, M. E., & Hamilton, V. E. (2010). A search for basaltic-to-intermediate glasses on Mars: Assessing martian crustal mineralogy. *Icarus*, 210, 135–149. <https://doi.org/10.1016/j.icarus.2010.06.028>
- Miyamoto, M. (1992). Infrared diffuse reflectance spectra of several thermally metamorphosed carbonaceous chondrites. *Proceedings of the NIPR Symposium on Antarctic Meteorites*, 5, 155–164.
- Morbidelli, A., Chambers, J., Lunine, J. I., Petit, J. M., Robert, F., Valsecchi, G. B., & Cyr, K. E. (2000). Source regions and timescales for the delivery of water to the Earth. *Meteoritics & Planetary Sciences*, 35, 1309–1320. <https://doi.org/10.1111/j.1945-5100.2000.tb01518.x>
- Nakamura, T. (2005). Post-hydration thermal metamorphism of carbonaceous chondrites. *Journal of Mineralogical and Petrological Sciences*, 100, 260–272. <https://doi.org/10.2465/jmps.100.260>
- Nakamura, T. (2006). Yamato 793321 CM chondrite: Dehydrated regolith material of a hydrous asteroid. *Earth and Planetary Science Letters*, 242, 26–38. <https://doi.org/10.1016/j.epsl.2005.11.040>
- Reuter, D. C., Simon, A. A., Hair, J., Lunsford, A., Manthripragada, S., Bly, V., et al. (2018). The OSIRIS-REx visible and infrared spectrometer (OVIRS): Spectral maps of the asteroid Bennu. *Space Science Reviews*, 214, 54. <https://doi.org/10.1007/s11214-018-0482-9>
- Rivkin, A. S. (2002). Hydrated minerals on asteroids: The astronomical record. *Asteroids III* (pp. 235–252).
- Rivkin, A. S., Davies, J. K., Johnson, J. R., Ellison, S. L., Trilling, D. E., Brown, R. H., & Lebofsky, L. A. (2003). Hydrogen concentrations on C-class asteroids derived from remote sensing. *Meteoritics & Planetary Sciences*, 1398, 1383–1398. <https://doi.org/10.1111/j.1945-5100.2003.tb00321.x>
- Rubin, A. E., Trigo-Rodríguez, J. M., Huber, H., & Wasson, J. T. (2007). Progressive aqueous alteration of CM carbonaceous chondrites. *Geochimica et Cosmochimica Acta*, 71, 2361–2382. <https://doi.org/10.1016/j.gca.2007.02.008>
- Ruff, S. W., Christensen, P. R., Barbera, P. W., & Anderson, D. L. (1997). Quantitative thermal emission spectroscopy of minerals: A laboratory technique for measurements and calibration. *Journal of Geophysical Research*, 102, 14899–14913. <https://doi.org/10.1029/97JB00593>
- Salisbury, J. W. (1993). Mid-infrared spectroscopy: Laboratory data. *Remote geochemical analysis: Elemental and mineralogical composition* (pp. 79–98). Cambridge University Press.
- Salisbury, J. W., D'Aria, D. M., & Jarosewich, E. (1991). Midinfrared (2.5–13.5  $\mu$ m) reflectance spectra of powdered stony meteorites. *Icarus*, 92, 280–297. [https://doi.org/10.1016/0019-1035\(91\)90052-u](https://doi.org/10.1016/0019-1035(91)90052-u)
- Salisbury, J. W., & Walter, L. S. (1989). Thermal infrared (2.5–13.5  $\mu$ m) spectroscopic remote sensing of igneous rock types on particulate planetary surfaces. *Journal of Geophysical Research*, 94, 9192–9202. <https://doi.org/10.1029/JB094iB07p09192>
- Schofield, P. F., Knight, K. S., Covey-Crump, S. J., Cressey, G., & Stretton, I. C. (2002). Accurate quantification of the modal mineralogy of rocks when image analysis is difficult. *Mineralogical Magazine*, 66(1), 189–200. <https://doi.org/10.1180/0026461026610022>
- Shirley, K. A., & Glotch, T. D. (2019). Particle size effects on mid-infrared spectra of lunar analog minerals in a simulated lunar environment. *Journal of Geophysical Research: Planets*, 124, 970–988. <https://doi.org/10.1029/2018JE005533>
- Simon, A. A., Kaplan, H. H., Hamilton, V. E., Lauretta, D. S., Campins, H., Emery, J. P., et al. (2020). Widespread carbon-bearing materials on near-Earth asteroid (101955) Bennu. *Science*, 370, <https://doi.org/10.1126/science.abc3522>
- Sugita, S., Honda, R., Morota, T., Kameda, S., Sawada, H., Tatsumi, E., et al. (2019). The geomorphology, color, and thermal properties of Ryugu: Implications for parent-body processes. *Science*, 364, 252. <https://doi.org/10.1126/science.aaw0422>
- Takir, D., & Emery, J. P. (2012). Outer main belt asteroids: Identification and distribution of four 3  $\mu$ m spectral groups. *Icarus*, 219, 641–654. <https://doi.org/10.1016/j.icarus.2012.02.022>

- Takir, D., Emery, J. P., & Mcsween, H. Y. (2015). Toward an understanding of phyllosilicate mineralogy in the outer main asteroid belt. *Icarus*, 257, 185–193. <https://doi.org/10.1016/j.icarus.2015.04.042>
- Takir, D., Emery, J. P., Mcsween, H. Y., Hibbitts, C. A., Clark, R. N., Pearson, N., & Wang, A. (2013). Nature and degree of aqueous alteration in CM and CI carbonaceous chondrites. *Meteoritics & Planetary Sciences*, 48. <https://doi.org/10.1111/maps.12171>
- Thomas, I. R., Bowles, N. E., Greenhagen, B. T., Glotch, T. D., Donaldson Hanna, K. L., Wyatt, M. B., et al. (2010). Emission measurements of lunar analogues for interpretation of returning data from the Diviner lunar radiometer on NASA's lunar reconnaissance orbiter. *41st lunar and planetary science conference*.
- Thomas, I. R., Greenhagen, B. T., Bowles, N. E., Donaldson Hanna, K. L., Temple, J., & Calcutt, S. B. (2012). A new experimental setup for making thermal emission measurements in a simulated lunar environment. *Review of Scientific Instruments*, 83, 124502. <https://doi.org/10.1063/1.4769084>
- Tomeoka, K., & Buseck, P. R. (1985). Indicators of aqueous alteration in CM carbonaceous chondrites: Microtextures of a layered mineral containing Fe, S, O and Ni. *Geochimica et Cosmochimica Acta*, 49, 2149–2163. [https://doi.org/10.1016/0016-7037\(85\)90073-0](https://doi.org/10.1016/0016-7037(85)90073-0)
- Tonui, E. K., Zolensky, M. E., Hiroi, T., Nakamura, T., Lipschutz, M. E., Wang, M.-S., & Okudaira, K. (2014). Petrographic, chemical and spectroscopic evidence for thermal metamorphism in carbonaceous chondrites I: CI and CM chondrites. *Geochimica et Cosmochimica Acta*, 126, 284–306. <https://doi.org/10.1016/j.gca.2013.10.053>
- Tonui, E. K., Zolensky, M. E., Lipschutz, M. E., Wang, M.-S., & Nakamura, T. (2003). Yamato 86029: Aqueously altered and thermally metamorphosed CI-like chondrite with unusual textures. *Meteoritics & Planetary Sciences*, 38, 269–292. <https://doi.org/10.1111/j.1945-5100.2003.tb00264.x>
- Tsuda, Y., Yoshikawa, M., Abe, M., Minamino, H., & Nakazawa, S. (2013). System design of the Hayabusa 2: Asteroid sample return mission to 1999 JU3. *Acta Astronautica*, 91, 356–362. <https://doi.org/10.1016/j.actaastro.2013.06.028>
- Vilas, F. (1994). A cheaper, faster, better way to detect water of hydration on solar system bodies. *Icarus*, 111, 456–467. <https://doi.org/10.1006/icar.1994.1156>
- Vilas, F., Jarvis, K. S., & Gaffey, M. J. (1994). Iron alteration minerals in the visible and near-infrared spectra of low-albedo asteroids. *Icarus*, 109, 274–283. <https://doi.org/10.1006/icar.1994.1093>
- Walsh, K. J., Morbidelli, A., Raymond, S. N., O'Brien, D. P., & Mandell, A. M. (2011). A low mass for Mars from Jupiter's early gas driven migration. *Nature*, 475, 206–209. <https://doi.org/10.1038/nature10201>
- Ziffer, J., Campins, H., Licandro, J., Walker, M. E., Fernandez, Y., Clark, B. E., et al. (2011). Near-infrared spectroscopy of primitive asteroid families. *Icarus*, 213, 538–546. <https://doi.org/10.1016/j.icarus.2011.04.008>
- Zolensky, M. E., Mittlefehldt, D. W., Lipschutz, M. E., Wang, M.-S., Clayton, R. N., Mayeda, T. K., et al. (1997). CM chondrites exhibit the complete petrologic range from type 2 to 1. *Geochimica et Cosmochimica Acta*, 61, 5099–5115. [https://doi.org/10.1016/S0016-7037\(97\)00357-8](https://doi.org/10.1016/S0016-7037(97)00357-8)